Authigenic carbonate and native sulfur formation in Messinian (upper Miocene) marine sediments: Sedimentological, petrographical and geochemical constraints

M. Natalicchio [a], D. Birgel [b], S. Giunti [c], L. Guibourdenche [d], L. Pellegrino [a], G. Aloisi [d], J. Peckmann [b], F. Dela Pierre [a],[*]

[a] Dipartimento di Scienze della Terra, Università di Torino, Via Valperga Caluso 35, 10125, Torino, Italy
[b] Institut für Geologie, Centrum für Erdsystemforschung und Nachhaltigkeit, Bundesstrasse 55, Universität Hamburg, 20146, Hamburg, Germany
[c] Institute of Geological Sciences, Polish Academy of Sciences, Ul. Twarda 51/55, 00-818, Warsaw, Poland
[d] Université de Paris, Institut de Physique du Globe de Paris, CNRS, 1 rue Jussieu, 75005, Paris, France

ABSTRACT

Carbonate concretions accompanied by elemental sulfur were found in an early Messinian (Late Miocene) marine succession of NW Italy. The rocks were studied with an integrated approach including sedimentological, petrographical, stable isotope (carbon, oxygen, and multiple sulfur isotopes), and lipid biomarker analyses. Unlike other examples from Messinian strata of the Mediterranean area, the studied carbonate and sulfur concretions did not derive from the diagenetic replacement of sulfate minerals. Three lithofacies were distinguished: a) laminated lithofacies representing aphotic carbonate stromatolites enclosing fossils of filamentous sulfide-oxidizing bacteria; b) brecciated lithofacies deriving from the brecciation of carbonate stromatolites by mud injections; c) sulfur-bearing lithofacies deriving from the precipitation of thin laminae of elemental sulfur at or close to the sediment-water interface. The carbon and oxygen stable isotope composition of authigenic carbonate minerals and lipid biomarkers indicate that the initial formation of the laminated lithofacies was favored by organoclastic sulfate reduction in the shallow subsurface close to the sediment-water interface, producing sulfide that sustained dense microbial mats of sulfide-oxidizing bacteria at the seafloor. Calcification of the mats and consequent formation of stromatolites were possibly favored by nitrate-driven sulfide oxidation at the seafloor. The subsequent brecciation of the stromatolites was apparently the consequence of sulfate-driven anaerobic oxidation of methane (SD-AOM) in an underlying sulfate-methane transition zone (SMTZ). Focused fluid flow from below, possibly resulting from destabilization of gas hydrates, was not only responsible for the brecciation of the stromatolites, but also for the delivery of bicarbonate ions and the consequent precipitation of additional, ^{13}C-depleted calcite (δ^{13}C values as low as −52‰). Along with bicarbonate, also hydrogen sulfide was produced by SD-AOM at the SMTZ and was transported upwards. The oxidation of hydrogen sulfide at or close to the seafloor promoted the formation of elemental sulfur characterized by δ^{34}S values and Δ^{33}S values close to coeval seawater sulfate.

1. Introduction

In marine sediments, the formation of authigenic carbonates and elemental sulfur can be induced by organoclastic sulfate reduction (OSR) and sulfate-driven anaerobic oxidation of methane (SD-AOM). OSR is a prominent pathway for organic matter remineralization in marine sediments (Jørgensen, 1982), where sulfate-reducing bacteria utilize porewater sulfate for the oxidation of organic matter, particularly short-chain carboxylic acids (e.g., Londry et al., 2004; Liu et al., 2020). Alternatively, sulfate can be reduced during SD-AOM in the sulfate-methane transition zone (SMTZ; e.g., Ritger et al., 1987; Akam et al., 2023). SD-AOM is performed by a consortium of methanotrophic archaea and sulfate-reducing bacteria (Boetius et al., 2000). Both OSR and SD-AOM produce bicarbonate ions that increase alkalinity (Ritger et al., 1987; Campbell, 2006; Akam et al., 2023). Along with bicarbonate production, hydrogen sulfide is produced by OSR (Jessen et al., 2016;

Himmler et al., 2018) and SD-AOM (Bohrmann and Torres, 2006; Campbell, 2006). Generally, free hydrogen sulfide can react with reduced iron to form pyrite (Berner, 1984), or can be reoxidized to sulfate or intermediate sulfur species including elemental sulfur (Jørgensen et al., 2004; Lin Q. et al., 2015; Lin Z. et al., 2018). The reoxidation of sulfide can be both an abiotic or biotic process. Abiotic oxidation proceeds with molecular oxygen or even in anoxic sediments, with the concomitant reduction of iron oxides (e.g., Lin Z. et al., 2018). Biotic oxidation of sulfide is mediated by different types of sulfide-oxidizing bacteria, which oxidize sulfide with oxygen (*Beggiatoa*) or nitrate (*Thioploca*; Teske and Nelson, 2006). Some sulfide-oxidizing bacteria (e.g., *Arcobacter*) are able to excrete sulfur, in turn promoting sulfur accumulation at or immediately below the seafloor (Taylor et al., 1999; Sahling et al., 2002; Wirsen et al., 2002; Sievert et al., 2007; Omoregie et al., 2008, 2009).

Generally, both OSR and SD-AOM produce ^{13}C-depleted bicarbonate; the carbon isotopic signature of authigenic carbonates can be used to differentiate between the two processes (Irwin et al., 1977; Peckmann and Thiel, 2004). While low δ^{13}C values (as low as −76‰) are characteristic for SD-AOM, higher values (approximately −20‰) may suggest that OSR was the dominant process responsible for bicarbonate production. Nevertheless, the carbon isotope signature of authigenic carbonates can be influenced by other carbon sources, including dissolved inorganic carbon (Irwin et al., 1977). Similarly, considering that the microbial sulfur pathways (sulfate reduction, sulfur disproportionation, sulfide oxidation) are partially associated with diagnostic sulfur fractionations, the sulfur isotope composition of elemental sulfur (^{32}S and ^{34}S), including the minor isotopes (^{33}S and ^{36}S) can be applied for distinguishing between sulfide produced by OSR and SD-AOM (Lin Z. et al., 2018; Liu et al., 2020, 2022) and potentially whether reoxidation
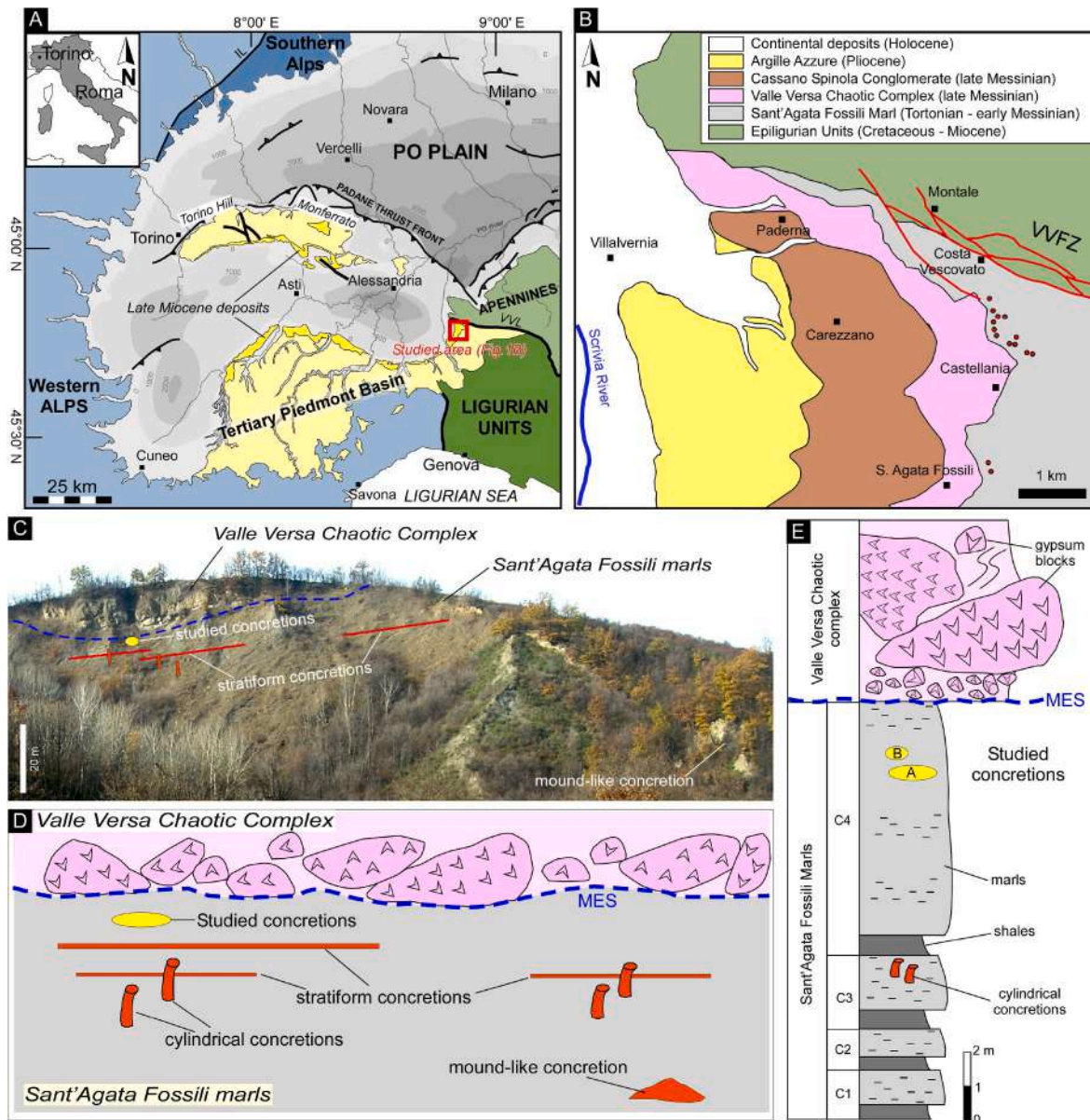

Fig. 1. A) Structural sketch map of the Tertiary Piedmont Basin (modified from Bigi et al., 1990). VVL: Villalvernia-Varzi Line. The red rectangle indicates the study area. B) Schematic geological map of the Ripa dello Zolfo area (modified from Festa et al., 2015). The red dots indicate the carbonate concretions. VVFZ: Villalvernia-Varzi fault zone. C) Outcrop view of the Ripa dello Zolfo section. The blue dotted line indicates the erosional surface at the base of the Valle Versa Chaotic complex (Messinian Erosional Surface; MES). D) Sketch showing the distribution of the carbonate concretions in the Ripa dello Zolfo area and the stratigraphic position of the concretions studied here. E) Stratigraphic log of the studied section, with indication of the lithologic cycles (C1–C4) and the concretions described in the text.

occurred biotically or abiotically (Guibourdenche et al., 2022). Additional information on the potential microbial processes involved in carbonate and native sulfur formation derives from the study of molecular fossils (lipid biomarkers), which are preserved in the authigenic mineral phases (Peckmann et al., 1999; Birgel et al., 2008; Natalicchio et al., 2012; Aloisi et al., 2013; Sabino et al., 2020; Rouwendaal et al., 2023).

In this paper we focus on unusual carbonate concretions associated with elemental sulfur that were found in the Tertiary Piedmont Basin (NW Italy), in the Ripa dello Zolfo (i.e., "Sulfur Scarp") section. The study was conducted integrating sedimentological, petrographical, carbon, oxygen, and multiple sulfur (δ^{34}S and Δ^{33}S) stable isotope analyses and is complemented with the study of molecular fossils. The Ripa dello Zolfo concretions are embedded in hemipelagic sediments of Messinian age. Carbonates associated with elemental sulfur are frequently reported from Messinian strata, but usually their genesis is associated with early (syngenetic) or late (epigenetic) replacement of preexisting sulfate minerals (Rouchy et al., 1998; Ziegenbalg et al., 2010; Caruso et al., 2015; Tzevahirtzian et al., 2022; Rouwendaal et al., 2023) that formed during the Messinian salinity crisis (Hsü et al., 1973; Ryan, 2023). Sulfate mineral dissolution by meteoric waters results in the release of calcium and sulfate ions. When organic compounds or hydrocarbons (methane, crude oil) are abundant, OSR or SD-AOM can induce the formation of authigenic carbonates and elemental sulfur (e. g., Peckmann et al., 1999; Lindtke et al., 2011; Aloisi et al., 2013; Caesar et al., 2019; Labrado et al., 2019; Rouwendaal et al., 2023). In great contrast, the Ripa dello Zolfo concretions formed prior to the Messinian salinity crisis and are not associated with sulfate minerals.

2. Geological and stratigraphic setting

The Tertiary Piedmont Basin is a wide wedge-top basin filled with Eocene to Messinian sediments that unconformably overlay a complex tectonic wedge of Alpine, Adriatic, and Ligurian units (Fig. 1A; Festa et al., 2005; Mosca et al., 2010; Rossi, 2017). The Ripa dello Zolfo section is located in the eastern part of the basin, south of the Villalvernia –Varzi line, a steeply dipping E-W striking regional fault separating the Northern Apennines to the north from the Tertiary Piedmont Basin to the South (Di Giulio and Galbiati, 1995; Ghibaudo et al., 1985; Festa et al., 2015). The stratigraphic succession of this sector consists of Oligocene-Pliocene sediments that unconformably overlay Mesozoic Ligurian units.

The older sediments exposed in the Ripa dello Zolfo section are the Sant'Agata Fossili Marls (Fig. 1B, C, D), consisting of Tortonian outer shelf sandstones and silty mudstones overlain by early Messinian slope hemipelagites and turbiditic sandstones (Ghibaudo et al., 1985). The hemipelagites consist of an alternation of organic-rich shales and marls (Fig. 1E), indicating cyclic fluctuation of oxygen levels at the seafloor under the control of precession-driven climate oscillations (Gennari et al., 2020; Pellegrino et al., 2020; Sabino et al., 2021). The hemipelagites host several stratabound carbonate concretions (Fig. 1C and D), considered to represent the product of methanogenesis and SD-AOM in the shallow subsurface (Natalicchio et al., 2012), cylindrical concretions interpreted to represent fluid conduits generated by the rising of methane-rich fluids toward the seafloor (Cavagna et al., 2015), and rare, isolated mound-like concretions of brecciated carbonates with dense accumulation of lucinid bivalves representing the product of fluid expulsion at the seafloor (Fig. 1C and D; Dela Pierre et al., 2010). Methane release was possibly favored by the destabilization of gas hydrates in the shallow subsurface (Dela Pierre et al., 2010). *In situ* gypsum deposits recording the onset of the Messinian salinity crisis are not observed in the study area. Gypsum exclusively occurs as meter-to tens of meter-sized blocks within a Messinian chaotic unit (Valle Versa Chaotic complex), which overlies the Sant'Agata Fossili Marls through an erosional surface (Messinian erosional surface; MES; Fig. 1B and C). This chaotic unit was emplaced by mass wasting events induced by an intra-Messinian tectonic phase (Clari et al., 2009; Natalicchio et al., 2013). It is in turn overlain by upper Messinian fluvial and lacustrine terrigenous deposits referred to as the Cassano Spinola Conglomerates (Ghibaudo et al., 1985, Fig. 1B). The Ripa dello Zolfo concretions studied herein were found in the topmost part of the Sant'Agata Fossili Marls, few meters below the erosional surface at the base of the Valle Versa Chaotic Complex (Fig. 1D and E).

3. Methods

3.1. Field and petrographic analyses

Field work included the logging of the stratigraphic section, the description of the geometry and lithology of the carbonate concretions, and their relationships with the loose consolidated host sediments. Twenty oriented samples of the carbonate concretions and eight samples from the host sediments were collected. All samples from the carbonate concretions were cut both parallel and perpendicular to bedding and the resulting slabs were observed under the microscope. Petrographic studies were performed at the Department of Earth Sciences of the University of Torino by examining 15 standard thin sections with plane- and cross-polarized as well as ultraviolet (UV) light microscopy. Cathodoluminescence (CL) observations were made using a CITL 8220 MK3 operating at ca. 17 kV and 400 μA. Scanning electron microscopy (SEM) observations were carried out on 30 carbon-coated sediment chips and ten thin sections using a JSM-IT300LV scanning electron microscope equipped with an energy dispersive X-ray spectroscope (EDS).

3.2. Carbon and oxygen stable isotope analyses of carbonate

Carbon (δ^{13}C) and oxygen (δ^{18}O) stable isotope analyses were conducted at the Department of Earth Sciences of the University of Milano on 24 samples (21 from the carbonate concretions and three from the unlithified sediments). About 200 μg of sample powder was microdrilled and subsequently reacted in an inert atmosphere (He) with ultra-pure concentrated orthophosphoric acid at 50°C using a Gasbench II (Thermo Fisher Scientific). The produced CO_2 was automatically flushed through a chromatographic column to the source of a Thermo Fisher Scientific Delta V Advantage isotopic ratio mass spectrometer (IR–MS). The carbon and oxygen isotope composition is expressed in the conventional delta notation calibrated to the Vienna Pee-Dee Belemnite (V-PDB) scale by the international standards IAEA 603 and NBS-18. Analytical reproducibility was better than ±0.1‰ for both δ^{13}C and δ^{18}O values.

3.3. Multiple sulfur isotope analyses of elemental sulfur

Multiple sulfur isotope analyses of elemental sulfur were conducted at the Institut de Physique du Globe de Paris. Powdered carbonate samples of ca. 1 g were reacted with pentane at room temperature to extract native sulfur. The dissolved sulfur was then reacted with activated copper that turned black to form Cu_xS_x. These steps were repeated several times until no Cu_xS_x formed anymore to ensure that all sulfur was successfully extracted from the samples. Cu_xS_x was then reacted under a nitrogen flux with an acidic $CrCl_2$ solution prepared daily following Fossing and Jørgensen (1989) to produce gaseous hydrogen sulfide. Produced hydrogen sulfide was precipitated into Ag_2S by bubbling into a $AgNO_3$ solution (Geng et al., 2018). The resulting Ag_2S was washed three times with deionized water and dried in an oven at 60 °C.

Ag_2S powder was subsequently reacted overnight in Nickel bombs with excess fluorine gas to produce gaseous SF_6. SF_6 was purified cryogenically and by gas chromatography before analysis by a dual inlet mass spectrometer MAT-253 (Ono et al., 2006; Johnston et al., 2007; Labidi et al., 2012). The δ^{34}S values were calibrated with an in-house SF_6 standard using the IAEAS-1 international standard (Robinson, 1995; Ding et al., 2001; Brand et al., 2014). Repeated analyses of IAEAS-1 (n =

4) yielded $\delta^{34}S = -0.26‰ \pm 0.1$ and $\Delta^{33}S = 0.086‰ \pm 0.005$. Replicate chemical extraction and measurement of the internal elemental sulfur standard (n = 2) yielded $\delta^{34}S = -7.97‰ \pm 0.1$ and $\Delta^{33}S = 0.027 \pm 0.002‰$. The major isotopic composition ($\delta^{34}S$) is expressed as the ratio between ^{34}S and ^{32}S abundances measured in the sample normalized by the same ratio in the international standard Vienna-Canyon Diablo Troilite (V-CDT) in per mil notation.

$$\delta^{34}S = \left(\frac{\frac{34_s}{32_{s\,sample}}}{\frac{34_s}{32_{s\,VCDT}}} - 1 \right) \times 1000 (‰) \tag{1}$$

The minor isotopic composition ($\Delta^{33}S$) is expressed as the deviation of the measured minor isotope partitioning ($^{33}S/^{32}S$) from predicted thermodynamic equilibrium calculated from $^{34}S/^{32}S$ measurement as follow (in per mil notation):

$$\Delta^{33}S = \delta^{33}S - 1000 \times \left[\left(1 + \frac{\delta^{34}S}{1000} \right)^{0.515} - 1 \right] (‰) \tag{2}$$

3.4. Lipid biomarker analyses

Analysis of the molecular fossil content of the Ripa dello Zolfo concretions was performed at the Institute for Geology, University of Hamburg, using the protocol described by Birgel et al. (2006). Three carbonate samples (ca. 200 g each) were crushed to small pieces and decalcified with 10% hydrochloric acid (HCl). The residual sediments after decalcification were subsequently saponified with 6% potassium hydroxide in methanol at 80°C for 2 h using an ultrasonic bath to release bound carboxylic acids and then extracted by ultrasonication with dichloromethane (DCM): methanol (3 + 1) until the extracts became colorless. Water was added to the combined extracts, and then 10% HCl was added to reach pH 1 to transfer the free fatty acids from the aqueous phase to the organic solvent phase. For gas chromatography (GC) analysis, each extract was cleaned by separation into *n*-hexane soluble and DCM soluble fractions. The *n*-hexane fraction was further treated and separated via solid phase extraction using a Supelco glass cartridge (6 ml, 500 mg, DSC-NH2) into four fractions of increasing polarity: (1) hydrocarbons with 4 ml *n*-hexane, (2) ketones with 6 ml *n*-hexane:DCM (3:1, v/v), (3) alcohols with 7 ml DCM:acetone (9:1, v/v), (4) carboxylic acids with 8 ml 2% formic acid in DCM. Alcohols were derivatized to trimethyl silyl ethers by reacting them with a 1:1 mixture of pyridine and N,O-bis(trimethylsilyl) trifluoroacetamide (BSTFA) at 70°C for 60 min. Free carboxylic acids were reacted with 1 ml 14% boron trifluoride in methanol at 70°C for 1 h to form fatty acid methyl esters. After cooling, the mixture was extracted four times with 2 ml *n*-hexane. Combined extracts were evaporated under a stream of nitrogen, and redissolved in *n*-hexane prior injection. The hydrocarbon fraction and the derivatized alcohol and carboxylic acid fractions were analyzed using coupled gas chromatography–mass spectrometry (GC–MS) with a Thermo Scientific Trace GC Ultra coupled to a Thermo Scientific DSQ II mass spectrometer. Internal standards used were 5α-cholestane for hydrocarbons, 1-nonadecanol and DAGE *n*-C$_{18}$/*n*-C$_{18}$ for alcohols, and 2-Me-C$_{18}$ fatty acid for carboxylic acids. Both GC systems were equipped with a HP-5 MS UI fused silica column (30 m × 0.25 mm i.d., 0.25 μm film thickness). The carrier gas was helium for GC–MS measurements. The GC temperature program for all fractions was: 50°C (3 min); from 50°C to 230°C (held for 3 min) at 25 °C/min; from 230°C to 325°C (held 20 min) at 6°C/min. Compound assignment was based on retention times and published mass spectral data. Compound-specific carbon isotope analyses were performed with an Agilent 6890 gas chromatograph coupled with a Thermo Finnigan Combustion III interface to a Thermo Finnigan Delta Plus XL isotope ratio mass spectrometer (GC-irms). The GC conditions were identical to those mentioned above for GC-FID and GC–MS analyses. Compound specific carbon isotope values are given as $\delta^{13}C$ values in per mil (‰) relative to the Vienna Pedee Belemnite (V-PDB).

3.5. Isotopic model

In order to better constrain the potential processes that shaped the isotopic composition of the Ripa dello Zolfo elemental sulfur, we designed a simple numerical model to reproduce the effect of mixing of different reduced sulfur pools, sulfate consumption by microbial sulfate reducers, and hydrogen sulfide oxidation. These processes can occur concomitantly in a sedimentary environment and modify the isotopic composition of elemental sulfur depending on their relative contribution. In this model, we fixed the $\delta^{34}S$-$\Delta^{33}S$ of the initial reacting sulfate processed by microbial sulfate reduction (MSR) with the average values of Messinian sea water (Masterson et al., 2016). First a Rayleigh distillation equation was used to model the evolution of the isotopic ratios of a first pool of hydrogen sulfide $^{3x/32}R_{H2S1} = ^{3x}S/^{32}S(H_2S1)$ produced by the progressive consumption of the sulfate reservoir $^{3x/32}RSO_4 = ^{3x}S/^{32}S$ (SO$_4$) by MSR, (with x = 33 or 34).

$$^{3x/32}R_{SO_4}(f_{SO_4}) = {}^{3x/32}R_{SO_4} (f_{SO_4} = 1) \, {}^*f_{SO_4}{}^{(\alpha MSR-1)} \tag{3}$$

$$^{3x/32}R_{H2}S1(f_{SO_4}) = ({}^{3x/32}R_{SO_4} (f_{SO4} = 1) - {}^{3x/32}R_{SO_4}(f_{SO4})^*f_{SO4}) /(1 - f_{SO4}) \tag{4}$$

In equations (3) and (4), f_{SO4} represents the fraction of the sulfate pool that remains in the pore water and varies between 0 (when the sulfate pool is completely exhausted) and 1 (corresponding to no change in sulfate concentration). We used a near thermodynamic equilibrium fractionation factor during microbial sulfate reduction $\alpha_{MSR} = 0.93$ ($\varepsilon_{MSR} = -70‰$) because microbial respiration generally occurs at low rates in marine settings (Jørgensen, 2021). Sensitivity tests for smaller fractionation factors ($\alpha_{MSR} = 0.96$ or $\varepsilon_{MSR} = -40‰$ and $\alpha_{MSR} = 0.98$ or $\varepsilon_{MSR} = -20‰$) during microbial sulfate reduction were also conducted (see Supplementary Fig. S1). We recalculated the isotopic composition of this first pool of hydrogen sulfide from the modelled isotopic ratios in equations (3) and (4) using equations (1) and (2) to obtain $\delta^{34}S_1$ and $\Delta^{33}S_1$.

We then mixed this first pool of sulfide ($\delta^{34}S_1$ and $\Delta^{33}S_1$) with a second pool of hydrogen sulfide (with isotopic values noted $\delta^{34}S_2$ and $\Delta^{33}S_2$) produced in the vicinity of the SMTZ, where f_{SO4} approaches 0 and $\delta^{34}S_2$ and $\Delta^{33}S_2$ values approach oceanic sulfate values. The following equation was used to model this mixing where parameter f_{mix} varying from 0 to 1 regulates the degree of mixing between the two pools of H$_2$S:

$$\delta^{3x}S_{mix} = \delta^{3x}S_1 \times f_{mix} + \delta^{3x}S_2 \times (1 - f_{mix}) \tag{5}$$

Finally, the hydrogen sulfide produced by the mixing of these two pools was reoxidized (biotically or abiotically). Fractionation factors for re-oxidation were taken from the literature (Zerkle et al., 2016; Eldridge and Farquhar, 2018).

4. Results

4.1. Field observations

The studied carbonate concretions are embedded in the topmost part of the Sant'Agata Fossili Marls, 3 m below the erosional contact with the Valle Versa Chaotic Complex (Fig. 2A). The sampled section consists of an alternation of laminated shales and marls, which defines four lithological cycles (C1, C2, C3 and C4; Fig. 1E), ranging in thickness from 1.20 m to 7.30 m.

Decimeter-sized cylindrical concretions cemented by dolomite are observed in the marls of cycle C3 (Fig. 1E and 2B). The carbonate concretions studied here (A and B) are hosted in the marls of cycle C4 (Fig. 2C and D). The concretions exhibit an ellipsoidal shape with sharp contacts with the hosting unconsolidated sediment. The width of concretion A is 1 m and its thickness is 50 cm (Fig. 2C); concretions B is thinner (20 cm) and the width is about 1 m (Fig. 2D). The marls hosting the concretions contain a relatively diversified foraminifer assemblage
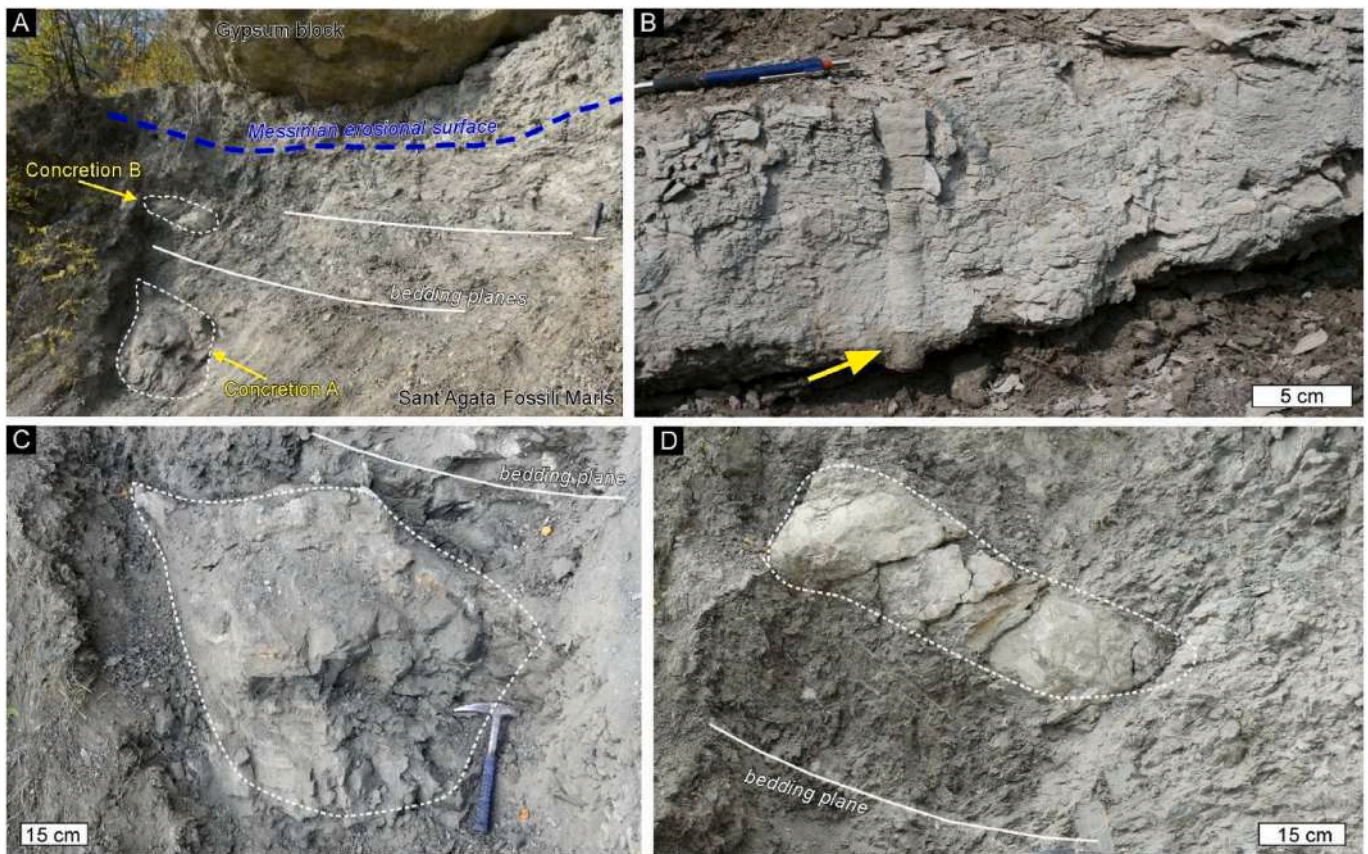
Fig. 2. A) Outcrop view of concretions A and B. The white lines indicate bedding, the blue dotted line the erosional surface at the base of the Valle Versa Chaotic Complex. B) A cylindrical concretion (yellow arrow) in the indurated marls of cycle C3. C) Outcrop view of concretion A. D) Outcrop view of concretion B.

that is commonly observed in pre-evaporitic Messinian sediments (e.g., Gennari et al., 2013). It includes both planktic (*Globigerinella obesa*, *Globigerina bulloides*, *Orbulina universa*, *Turborotalita quinqueloba*) and benthic (*Cibicidoides* spp., *Valvulineria complanata*, *Melonis* spp., *Hanzawaia boueana*, *Bulimina echinata*, *Bulimina aculeata*, *Boliviva spathulata*) taxa (R. Gennari, personal communication). In the absence of detailed bio-and cyclostratigraphic analyses that are beyond the scope of this paper, no conclusive age constraints are available for the studied sediments. However, some evidence is provided by benthic foraminifers. In particular: a) the relatively diversified assemblage described above is similar to the assemblage that in the nearby astronomically-dated Govone section was observed in sediments deposited between 6.6 and 6.4 Ma (Gennari et al., 2020), which is the age suggested for the studied Ripa dello Zolfo sediments; b) such an age assignment agrees with the presence of *Bulimina echinata* just below concretion A, which indicates an early Messinian age (younger than 6.7 Ma) and poorly oxygenated bottom water conditions (Violanti, 1996).

4.2. Sedimentology and petrography

Three lithofacies of the Ripa dello Zolfo concretions were distinguished on the basis of sedimentological and petrographical features: a) laminated lithofacies; b) brecciated lithofacies; c) sulfur-bearing lithofacies. The brecciated and sulfur-bearing lithofacies are further characterized by irregular cavities, partially filled with calcite.
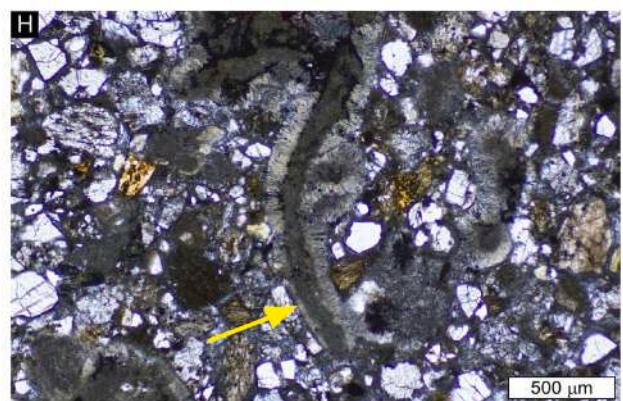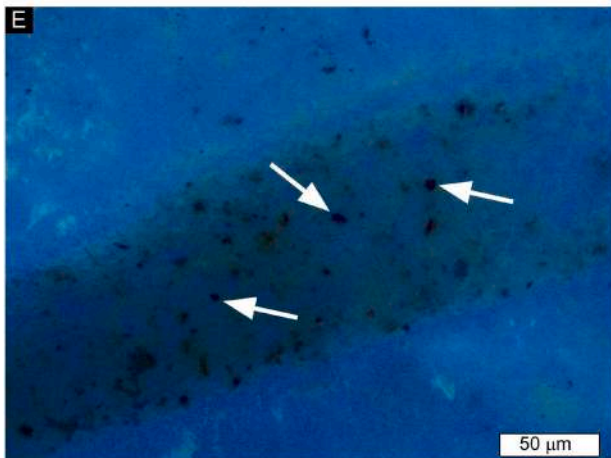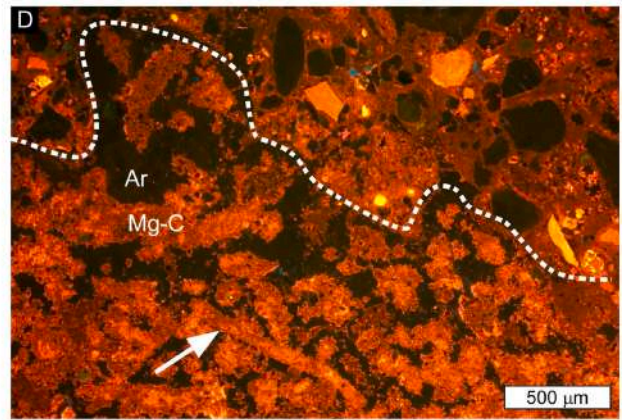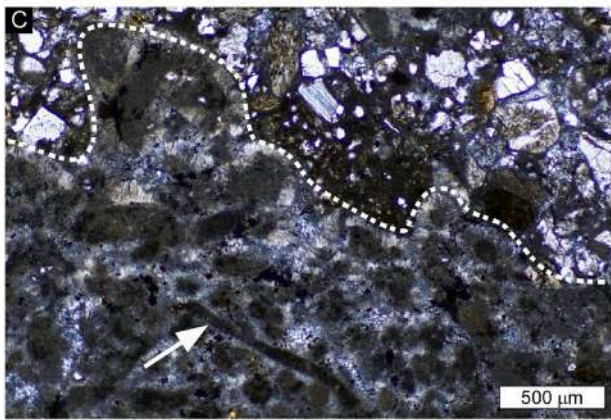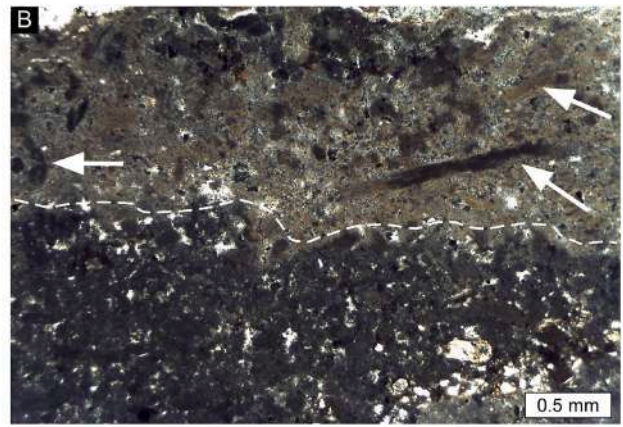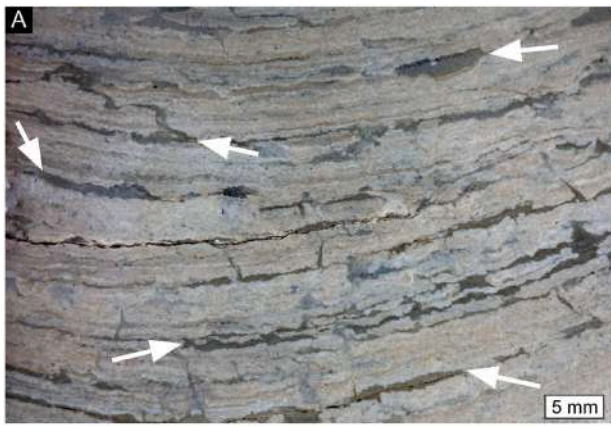
4.2.1. Laminated lithofacies
This lithofacies is represented by concretion B and is typified by a lamination defined by the alternation of mm-thick yellow laminae and thinner gray to brownish discontinuous laminae (Fig. 3A and B). Both types of laminae are composed of peloids and curved to straight

filamentous microfossils 70–100 μm in diameter and up to 1 mm in length (Fig. 3C). Pyrite framboids are common. In the gray to brownish laminae, filaments are densely packed, whereas in the yellow laminae filaments are sparse (Fig. 3B). Laminae are cemented by a low-Mg calcite microspar with yellow to bright orange CL color. This cement is also observed within the filamentous microfossils (Fig. 3D). The latter show a bright autofluorescence when exposed to UV light, suggesting high contents of organic matter, and contain tiny opaque grains corresponding to iron sulfides (Fig. 3E). Interestingly, in the yellow laminae most filaments and peloids are rimmed by a 100 μm-thick layer of fibrous aragonite, not luminescent under CL (Fig. 3D). In these laminae, aragonite crystals also fill residual porosity. Rare, thin white laminae composed of acicular crystals of aragonite are also present; they appear locally dark in transmitted light because of the presence of fluid inclusions and organic matter. The filament-bearing laminae are crosscut by a complex network of mm-wide fissures oriented both parallel and at a high angle with respect to bedding (Fig. 3A–F). These features may cause brecciation of the originally laminated fabric, which can be locally completely disrupted (Fig. 3F). The fissures are filled with foraminifer-bearing hemipelagic mud sourced from the Sant'Agata Fossili Marls, sand-sized terrigenous grains (quartz, mica flakes, carbonates), filamentous microfossils, and angular clasts of aragonite (Fig. 3G and H). Clasts are commonly aligned parallel to the fissure walls. The mud infill is cemented by a calcite microspar with dark orange CL color, different from the color of the cement observed in the filament-rich laminae (Fig. 3D).

4.2.2. Brecciated lithofacies
The brecciated lithofacies was identified in concretion A, where it is interbedded with the sulfur-bearing lithofacies (Fig. 4A and B). It consists of mm-to cm-sized angular clasts composed of dense accumulations

(caption on next page)

Fig. 3. A) Polished slab of the laminated lithofacies (cut perpendicular to bedding). Note the whitish/yellowish finely laminated packets and mud-filled fissures (arrows) orientated both parallel and at a high angle with respect to lamination. B) Two filament-bearing laminae. The white dotted line is the boundary between a lamina with densely packed filaments (below) and a lamina with sparser filaments (above). The arrows indicate filaments in the upper lamina. C) Irregular boundary (white dotted line) between a filament and peloid-bearing lamina and a mud-filled fissure with abundant terrigenous grains. The white arrow in the lower part points to a filament. D) Cathodoluminescence (CL) image of C. Note the different CL color of the cement in the filament and peloid-bearing lamina (bright orange) and in the mud-filled fissure (dark orange). Aragonite (Ar) is non luminescent. Mg–C: low magnesium calcite. The white arrow in the lower part points to a filament. E) Detail of a fluorescent filament. The white arrows indicate tiny opaque grains corresponding to iron sulfide grains. F) Close up of the laminated lithofacies (polished slab cut perpendicular to bedding). Note the mud filled fissures (arrows) and the brecciation of the laminated fabric. G, H) Details of a mud filled fissure. Note in G the clasts composed of aragonite and in H the filament rimmed by aragonite (yellow arrow) and the abundant terrigenous grains.

B, C, G, H: plane-polarized photomicrographs; E: cathodoluminescence photomicrograph; H: ultraviolet-light photomicrograph.

of filamentous microfossils rimmed by aragonite (Fig. 4C), identical to those described in the laminated lithofacies. The matrix between the filaments is cemented by the same low-Mg calcite microspar cementing the filaments. Calcite has the same bright orange CL color as in the laminated lithofacies (Fig. 4D). The clasts commonly reveal a fitted fabric and display an isopachous rim of fibrous aragonite composed of mm-long acicular crystals, which are not luminescent under CL (Fig. 4C and D). The same network of mud-filled fissures described in the laminated lithofacies is observed. Here, however, the degree of brecciation is higher than in the laminated lithofacies and the original fabric is completely disrupted. The brecciated lithofacies is characterized by irregular and elongated cavities, locally with angular edges, ranging in size from some mm to a few cm, in places filled with calcite (Fig. 4E). Some cavities show an internal segmentation defined by the branching of micritic films of putative microbial origin, in turn covered by calcite microcrystals (Fig. 4F).

4.2.3. Sulfur-bearing lithofacies

This lithofacies is observed in concretion A, sandwiched between the brecciated lithofacies. It consists of a 2 cm thick interval formed by mm-thick pale-yellow, sulfur-rich discontinuous laminae intercalated to a dark gray and brownish sediment (Fig. 4B and 5A). The yellow laminae seal the mud-filled fissure on the underlying brecciated lithofacies but locally laminae are bent upward or crosscut by the same mud-filled fissures observed in the breccia (Fig. 4B). In plane view, sulfur forms cm-large patches that interfinger with the dark gray sediment and the brecciated lithofacies (Fig. 5B). Under transmitted light, the sulfur laminae appear dark and show a core consisting of thin flakes of native sulfur (Fig. 5C), embedded in a micritic sediment composed of micron-sized calcite crystals mixed with sulfur. Calcite shows the same dark orange-brown CL color as the calcite observed in the mud-filled fissures. The thin native sulfur flakes show a bright autofluorescence, in contrast to the poorly fluorescent micrite with scattered sulfur (Fig. 5D). The fluorescent sulfur consists of irregular filamentous or coccoidal objects (10 μm across and up to 50 μm long; Fig. 5E), which are interpreted as putative microbial features. Millimeter-sized elongated cavities parallel to lamination and partially filled with calcite crystals enclosing micron-sized sulfur grains were observed in the sulfur-bearing lithofacies (Fig. 5F, G, H).

4.3. Carbon and oxygen stable isotopic composition of carbonates and multiple sulfur isotopic composition of elemental sulfur

The laminated lithofacies shows clustered carbon and oxygen isotope values of both calcite and aragonite cements with $\delta^{13}C$ values ranging from − 23.5 to −14.9‰ and $\delta^{18}O$ values ranging from −1.4 to +1.3‰; only one sample of aragonite cement shows more positive $\delta^{13}C$ (−1.6‰) and $\delta^{18}O$ (+5.2‰) values (Fig. 6 and Table 1). Three filament-bearing clasts in the brecciated lithofacies were analyzed; $\delta^{13}C$ values range from −20.4 to −10.8‰ and $\delta^{18}O$ values from +1.6 to +5.7‰. The microcrystalline calcite of the mud-filled fissures in the brecciated lithofacies displays similar $\delta^{18}O$ values (+2.5‰ on average), but is significantly more ^{13}C-depleted ($\delta^{13}C$ from − 52 to −30‰). Similar $\delta^{13}C$ values (−30.5‰) characterize the calcite cement enclosing sulfur in the sulfur-bearing lithofacies. Its $\delta^{18}O$ values are around +0.7‰ on average.

The results of sulfur isotope analyses of elemental sulfur from the sulfur-bearing lithofacies are shown in Table 2 and Fig. 7. The $\delta^{34}S$ values range from 10.4 to 12.2‰, whereas the $\Delta^{33}S$ values fall between 0.054 and 0.068‰.

4.4. Lipid biomarker data and compound specific carbon isotopes

4.4.1. Hydrocarbons

In all three lithofacies, hydrocarbons are present with low contents (Supplementary Fig. S2). In the laminated lithofacies, long-chain *n*-alkanes (C_{27-33}) are the most abundant compounds; other compounds are short-chain *iso*-alkanes with 18 and 19 carbons. In great contrast, the brecciated and sulfur-bearing lithofacies are typified by only minor contents of alkanes, but high contents of native sulfur in the brecciated lithofacies. Long-chain alkanes yielded $\delta^{13}C$ values ranging from −34 to −32‰, which is typical for leaf waxes of land plants.

4.4.2. Alcohols

The three lithofacies are characterized by a different lipid assemblage in the alcohol fraction (Fig. 8). The laminated lithofacies is predominated by *n*-alcohols with chain lengths peaking from C_{24} to C_{26} (Fig. 8A). Other abundant compounds are land-plant derived pentacyclic triterpenoids (oleanenes; Killops and Frewin, 1994) and two dinostanol epimers, most likely derived from dinoflagellates (e.g., Volkman, 2003). Other, minor compounds were three non-isoprenoid macrocyclic glycerol diethers (McDGs), which were first described in authigenic carbonates from Egypt and Spain (Baudrand et al., 2010). These compounds are accompanied by the isoprenoid diphytanyl glycerol diether archaeol, which is a common membrane lipid of many archaea, especially of methanogenic, methanotrophic, and halophilic archaea (Koga et al., 1998; Blumenberg et al., 2004 Dawson et al., 2012). The brecciated lithofacies predominantly contains mid-to long-chain *n*-alcohols, with a predominance of even over odd chains that are maximizing at chain lengths from C_{24} to C_{28} (Fig. 8B). In contrast to the laminated lithofacies, the two dinostanols are accompanied by cholesterol, cholestanol, $\beta-$sitosterol, stigmastanol and other minor sterols in the brecciated lithofacies. Further, various $\alpha,\omega-$diols and 1,15-C_{30}-diol are present; the latter are commonly assigned to eustigmatophyte algae (e.g., Rampen et al., 2022). Other minor compounds are dialkyl glycerol diethers (DAGEs) with 31–33 carbons. Similar as for the laminated lithofacies, three non-isoprenoid macrocyclic glycerol diethers (McDGs) were found in brecciated lithofacies, but with slightly higher contents, also accompanied by archaeol (Fig. 8B). The sulfur-bearing lithofacies shows the same composition of *n*-alcohols and various sterols and stanols as in the brecciated lithofacies (Fig. 8C). In contrast to the other lithofacies, the three non-isoprenoid McDGs are the predominating compounds in sulfur-bearing lithofacies; for all lithofacies, C_{34}-McDG (compound C; Fig. 8C) is most abundant and C_{32}-McDG (compound A, Fig. 8C) is least abundant (Fig. 8C and D). Compound specific carbon isotope compositions of McDGs in the sulfur-bearing lithofacies range from −31 to −27‰; in the other samples, McDGs contents were too low to measure their isotopic compositions. DAGEs were found as well, comprising $C_{31/32}$ DAGEs with average $\delta^{13}C$ values of −39‰ (Fig. 8C). The $\delta^{13}C$ values of stanols range from −29‰ (stigmastanol) to −23‰ (dinostanol); however, some sterols co-elute with long-chain *n*-alcohols.
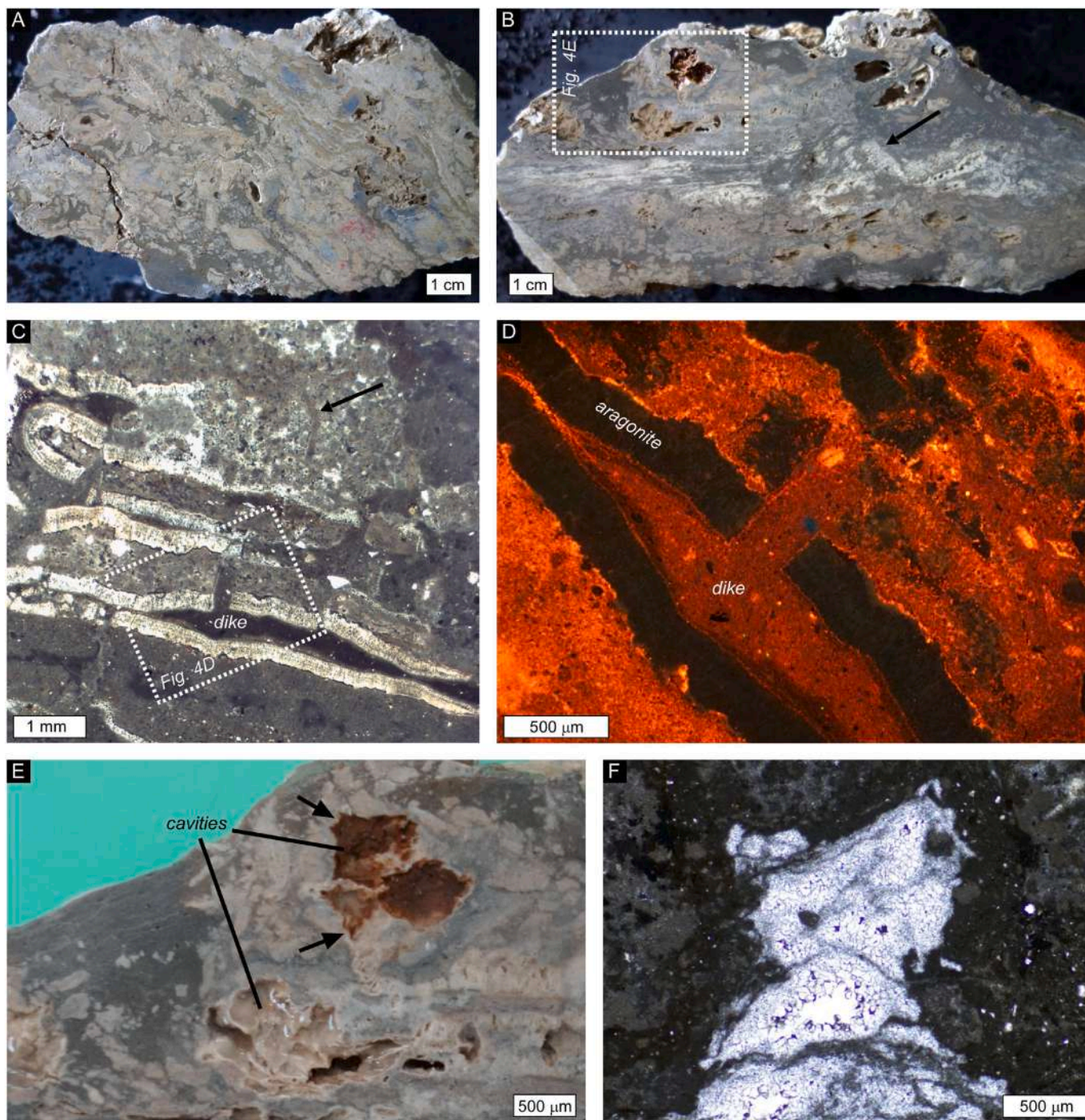
Fig. 4. A, B) Polished slabs of the brecciated and sulfur-bearing lithofacies. A) Brecciated lithofacies; note the whitish angular clast and the fissure-filling dark gray mudstone. B) Sulfur-bearing lithofacies (cut perpendicular to bedding). Discontinuous sulfur rich-yellowish laminae are interbedded between the brecciated lithofacies. Note that the sulfur-rich laminae are locally bent upward and crosscut by gray mudstones (arrow). The rectangle indicates the location of Fig. 4E. C) Clasts with an isopachous rim of aragonite. Clasts are separated by fissure-filling mudstone. Some filaments in a clast (arrow). The rectangle indicates the location of Fig. 4D. D) Detail of C under cathodoluminescence light (CL), showing a mud-filled fissure cross cutting the clasts. Note the different CL color of the microcrystalline cement in the clasts (bright orange) and in the mudstone (dark orange). The aragonite rim of the clasts is non luminescent. E) Detail of B (polished slab cut perpendicular to bedding). Note irregular cavities partially filled with cement. Some cavities display angular edges (arrows). F) Detail of a cavity, partially filled with calcite crystals. Note the internal segmentation evidenced by the branching of thin micritic filaments. C, F: plane-polarized photomicrographs; D: cathodoluminescence light photomicrograph.

Archaeol yielded a $\delta^{13}C$ value of $-19‰$, representing the least ^{13}C-depleted compound (Supplementary Table S1).

4.4.3. Carboxylic acids

The carboxylic acid fractions are dominated by *n*-fatty acids for all lithofacies (Supplementary Fig. S3). In particular, mid-to long-chain *n*-fatty acids with 22–30 carbon atoms predominate in the brecciated lithofacies. In the laminated carbonate and sulfur-bearing lithofacies additionally high contents of saturated C_{14-18} *n*-fatty acids have been recognized. The $\delta^{13}C$ values of C_{16-18} *n*-fatty acids are $-28‰$ on average,
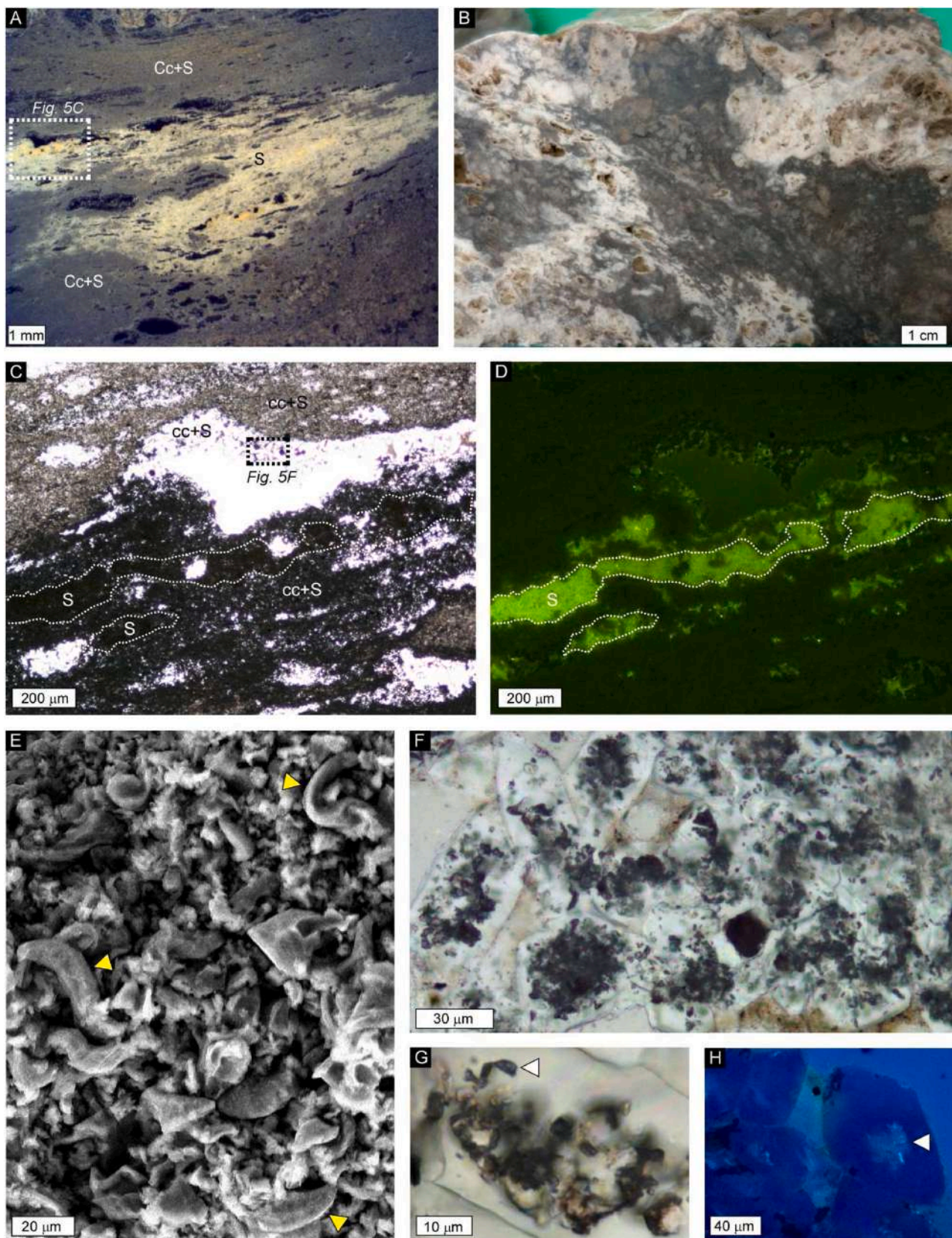
Fig. 5. A) Sulfur-rich laminae (S) interbedded to dark-gray brownish fine-grained sediment consisting of sulfur and calcite microspar (Cc + S). B) Sulfur patches interfingering with a breccia composed of filament-bearing clasts. Polished slab (cut parallel to bedding). C) Irregular flakes of elemental sulfur (S). Cc + S: Calcite ad sulfur. The black rectangle indicates the location of Fig. 5F. D) Fluorescent sulfur flakes (S). E) Irregular elongated sulfur grains (arrows). F) Detail of C: sulfur grains enclosed in calcite microcrystals partially filling an irregular cavity. G) Detail of F, showing an irregular, elongated sulfur grain resembling a filament (arrow). H) Fluorescent sulfur grain (arrow). A: reflected light photomicrograph; C, F, G: plane-polarized light photomicrographs; D, H: ultraviolet-light photomicrographs.; E: SEM photomicrograph.
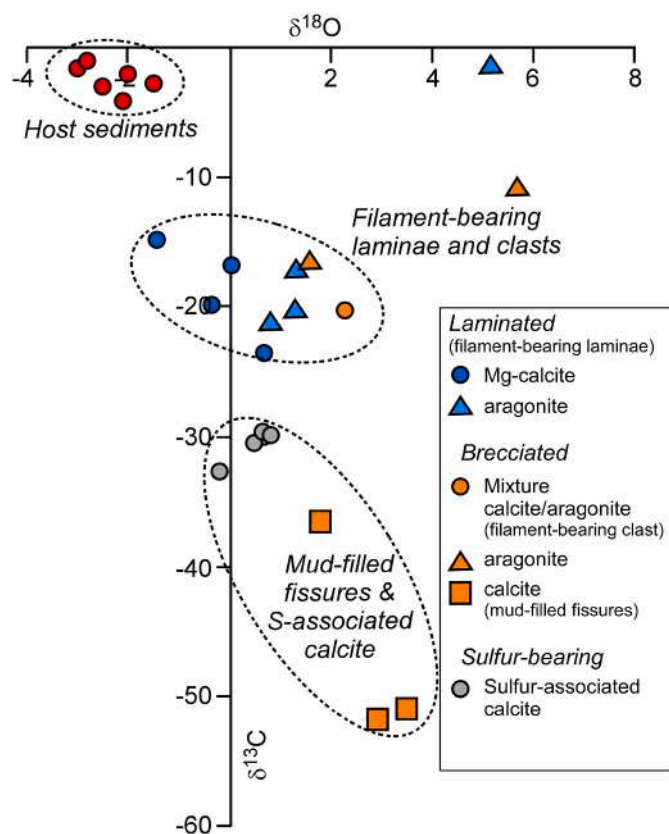
Fig. 6. Cross-plot of the carbon and oxygen stable isotope data of the studied concretions. Data from the host unconsolidated sediments are from Natalicchio et al. (2012).

Table 1
Carbon (δ^{13}C) and oxygen (δ^{18}O) stable isotope values.

Lithofacies	Sample	Mineralogy	δ^{13}C [‰PDB]	δ^{18}O [‰PDB]
Laminated	X.4.1	Mg calcite	−19.9	−0.4
	X.4.3	Mg calcite	−14.9	−1.4
	X.4b	Mg calcite	−16.7	+0.1
	X.8.2	Mg calcite	−23.5	+0.7
	X.4.2	Aragonite	−17.0	+1.3
	X.4.4	Aragonite	−1.6	+5.2
	X.4a	Aragonite	−21.4	+0.8
	X.8.1	Aragonite	−20.3	+1.3
Brecciated	X2a.3	Calcite	−50.8	+3.5
	X2a.4	Calcite	−36.6	+1.8
	X2a.4	Calcite	−36.5	+1.8
	X.2.1	Calcite	−52.0	+2.9
	X.2a.2	Calcite/aragonite	−20.4	+2.3
	X.2a.1	Aragonite	−10.8	+5.7
	X.2.2	Aragonite	−16.6	+1.6
Sulfur-bearing	X.3.I	Calcite	−30.0	+0.6
	X.3.II	Calcite	−30.2	+0.8
	X.3.IV	Calcite	−30.6	+0.5
	X.3.V	Calcite	−29.9	+0.8
	X.3.V	Calcite	−29.9	+0.7
	X.3.III	Calcite	−32.7	−0.2
Encasing marls	DM133	Calcite	−4.1	−2.1
	DM134	Calcite	−1.7	−3.0
	DM135	Calcite	−1.1	−2.8
	OM1	Calcite	−2.8	−1.5
	OM3	Calcite	−2.1	−2.0
	OM9	Calcite	−3.0	−2.5

whereas longer chain *n*-fatty acids range from −28‰ (*n*-C$_{22}$) and −31‰ (*n*-C$_{28}$). Acyclic biphytanic diacid yielded a value of −31‰. All samples revealed minor amounts of 10Me–C$_{16}$ and *iso*- and *anteiso*- C$_{15}$ and C$_{16}$

Table 2
Multiple sulfur isotope data from elemental sulfur.

Sample name	δ^{34}S ± 0.1‰	Δ^{33}S ± 0.002‰
X.3c1	12.2	0.067
X.3c2	11.7	0.054
X.3d1	11.1	0.064
X.3d2	10.4	0.062
X.3e	11.3	0.068

fatty acids. The low contents of these compounds, however, did not allow for their compound-specific carbon isotope composition to be determined.

5. Discussion

5.1. The laminated lithofacies: A carbonate stromatolite reflecting organoclastic sulfate reduction

The laminated lithofacies displays a characteristic stromatolitic fabric resulting from the vertical stacking of filament-rich laminae. The intricate network of fluorescent filamentous structures supports its microbial origin. The affiliation of the fossilized filamentous structures to a specific group of microorganisms is difficult (Schopf et al., 2012; Dela Pierre et al., 2015; Andreetto et al., 2019), since different clades of prokaryotes, including cyanobacteria and sulfide-oxidizing bacteria, can produce similar morphological features.

The studied rocks are enclosed within unlithified hemipelagic sediments deposited on a poorly oxygenated seafloor well below the photic zone; i.e., in the medium-lower bathyal zone between 500 m and 1000 m estimated water depth (Ghibaudo et al., 1985). Such depth constraints exclude that the formation of the microbialite was mediated by phototrophic microorganisms. The large diameter (~80 μm) and the curved shape of filaments, as well as the presence of tiny iron sulfide grains within them (Fig. 3E) – the latter possibly corresponding to early diagenetic transformation products of original sulfur globules stored by the bacteria – suggest that the filaments probably represent remains of large sulfide-oxidizing bacteria like *Beggiatoa* or *Thioploca* (cf. Oliveri et al., 2010; Dela Pierre et al., 2015; Andreetto et al., 2019; Aloisi et al., 2022). Such an assignment agrees with the presence of saturated C$_{14}$, C$_{16}$, and C$_{18}$ fatty acids as well as monounsaturated C$_{18:1\omega7}$ fatty acids in the studied samples. Although these compounds are ubiquitous and therefore can derive from a wide array of organisms among bacteria and eukaryotes, they are the most common lipids found in modern chemotrophic microbial mats dominated by *Beggiatoa* and *Thioploca* (McCaffrey et al., 1989; Arning et al., 2008).

The excellent preservation of the filamentous microfossils, showing circular cross sections without any evidence of compaction, is the consequence of rapid precipitation of carbonate minerals stabilizing the soft microbial mat. The biogeochemical processes, favoring carbonate precipitation and coming along with the concomitant production of hydrogen sulfide apparently sustaining sulfide-oxidizing bacteria at the seafloor, were probably OSR and SD-AOM (cf. Irwin et al., 1977; Peckmann and Thiel, 2004). However, subsequent sulfide oxidation with oxygen promotes a decrease of alkalinity, favoring dissolution of carbonate minerals (Peckmann et al., 2004; Bailey et al., 2009; Himmler et al., 2018). In contrast, acidity can be consumed and calcification can be stimulated if sulfide-oxidizing bacteria couple the oxidation of sulfide with the reduction of nitrate, following the reaction HS$^-$ + NO$_3^-$ + H$^+$ + H$_2$O → SO$_4^{2-}$ + NH$_4^+$ (Bailey et al., 2009; Himmler et al., 2018). Nitrate-dependent sulfide oxidation therefore may have induced an increase of alkalinity and the consequent precipitation of carbonate minerals in the Ripa dello Zolfo microbial mat. This process has been described in modern stromatolitic carbonates at a deep-water methane seep located in the oxygen minimum zone of the northern Arabian Sea (Himmler et al., 2018). There, *Thioploca* filaments are surrounded by
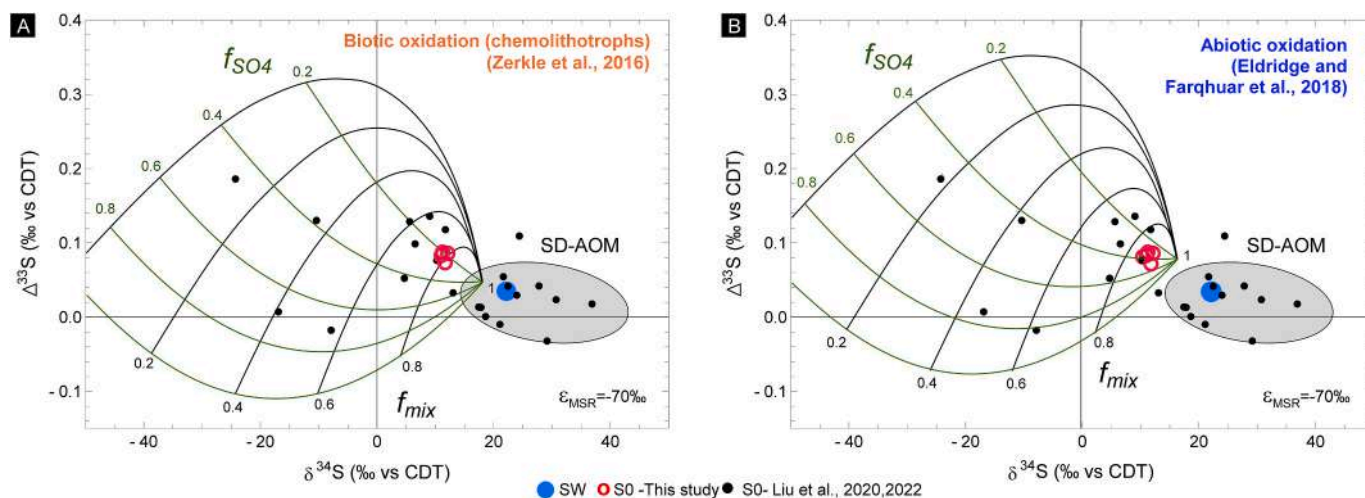
Fig. 7. Multiple sulfur isotope composition (δ^{34}S and Δ^{33}S) of elemental sulfur of the studied concretions and modelled isotope composition for biotic (A) and abiotic (B) oxidation of H_2S. Individual curves correspond to the modelled isotopic composition of the elemental sulfur resulting from the oxidation of H_2S. The latter formed by mixing of two isotopically distinct pools. The first pool is produced by the progressive consumption of SO_4^{2-} in the porewater, regulated by the parameter f_{SO4} ($f_{SO4} = 1$ meaning that no SO_4^{2-} has been consumed by microbial sulfate reduction and $f_{SO4} = 0$ meaning that all the porewater SO_4^{2-} has been reduced to H_2S). The second pool of H_2S is produced at the vicinity of the SMTZ where all SO_4^{2-} has been consumed by microbial sulfate reduction and its isotopic composition is close to the seawater sulfate isotopic value (i.e δ^{34}S = 22.2‰ and Δ^{33}S = 0.035‰). f_{mix} is the parameter that regulate the mixing of the two pools of H_2S and vary between 0 and 1, with $f_{mix} = 0$ meaning that all the S^0 was produced by the oxidation of the first pool of H_2S and $f_{mix} = 1$ meaning that all the S^0 was produced by the oxidation of H_2S produced at the vicinity of the SMTZ (pool 2).

and partially filled with fibrous aragonite (Himmler et al., 2018).

In the Ripa dello Zolfo concretions, carbonate minerals are represented by: a) low-Mg calcite microspar found within the filaments and in the enclosing matrix; b) aragonite, mostly encrusting filaments. The moderately negative δ^{13}C values (~ -20‰) of the carbonate and the presence of *iso-* and *anteiso-*C_{15} fatty acids and 10Me–C_{16} fatty acids, compounds commonly associated with sulfate-reducing bacteria in marine environments (Arning et al., 2008, 2009), suggest that carbonate precipitation and generation of sulfide was induced by OSR in organic-rich sediments (Fig. 9A). In addition, most of the δ^{18}O values ($-1.4 < \delta^{18}$O ‰ PDB $< +1.3$) are indicative of open marine conditions (Bellanca et al., 2001; Pierre and Rouchy, 2004). The depositional environment of the Ripa dello Zolfo concretions was therefore different from the hypersaline environment that favored the formation of similar stromatolitic carbonates from Sicily (Oliveri et al., 2010) and Calabria (Perri et al., 2017; Borrelli et al., 2021). The latter carbonates originated during the Messinian salinity crisis and are characterized by more positive δ^{18}O values (from +3 to +5 ‰PDB; Perri et al., 2017) than the carbonates of the laminated lithofacies of the Ripa dello Zolfo concretions.

The alternation of laminae with less (yellow laminae) and more (gray laminae) filamentous microfossils observed in the Ripa dello Zolfo concretion might suggest changing redox conditions at the seafloor, most likely controlled by short-term climate fluctuations (Fig. 9B and C). Under low oxygen bottom water conditions, the seafloor was colonized by microbial mats possibly dominated by filamentous sulfide-oxidizing bacteria (e.g., *Thioploca)* sensitive to high concentrations of molecular oxygen (Jørgensen and Gallardo, 1999*)*. At the sediment water interface, the presence of hydrogen sulfide produced by OSR promoted nitrate-driven sulfide oxidation that favored the precipitation of aragonite around the filaments (Fig. 9B). Just below the mat, active OSR in anoxic pore waters, induced the precipitation of low-Mg calcite microspar, contributing to the stabilization of the mats. When the conditions at the seafloor changed to higher oxygen levels, and the sulfate reduction zone moved downward in the sedimentary column, sulfide-oxidizing bacteria retreated into the sediments where sulfide was still available. Such a process possibly resulted in the formation of the laminae with more densely spaced filaments (darker laminae; Fig. 9C).

5.2. The brecciated lithofacies: stromatolite disruption induced by deep-seated SD-AOM

The clasts of the brecciated lithofacies display the same composition (filamentous microfossils rimmed by aragonite and cemented by low-Mg calcite) and carbon and oxygen isotope values as the laminated lithofacies (Fig. 6). This pattern suggests that brecciation occurred at the expense of an already consolidated microbial mat formed under similar conditions as described for the laminated lithofacies (Fig. 9A–D). The sharp edges of the clasts and their fitted, jigsaw puzzle pattern indicate that brecciation occurred in situ. In addition, the fact that the clasts are separated by mud-filled fissures suggests that brecciation was caused by the injection of fluidized mud during its rise through the semi-lithified microbial mat. Mud injections have also been recognized in Triassic methane-seep deposits, suggesting that high enough pore-water pressures are attained in gas-rich sediments to force fluid mud into carbonate lithologies at shallow depth (Peckmann et al., 2011). Cementation of the microbial mats was promoted by OSR and nitrate-driven sulfide oxidation at or immediately below the seafloor, creating a rigid barrier favoring local overpressure conditions. The same process also affected the laminated lithofacies, even though the degree of brecciation of the latter is lower than in the brecciated lithofacies.

Interestingly, the calcite cement of the mud-filled fissures displays δ^{13}C values as low as −52‰. The same cement is typified by more positive δ^{18}O values (+2.5‰ on average), compared to the laminated lithofacies (+1.0‰ on average). The ^{13}C depletion indicates that the bicarbonate incorporated into the authigenic calcite derived from the oxidation of biogenic methane by SD-AOM (Peckmann and Thiel, 2004), Similar δ^{13}C values were found in the Ripa dello Zolfo area for strata-bound, cylindrical, and mound-like concretions (Dela Pierre et al., 2010; Natalicchio et al., 2012), occurring only a few meters below the concretions studied herein (Fig. 9A). The positive δ^{18}O values of these concretions (up to 8 ‰) possibly reflect gas hydrate destabilization (Dela Pierre et al., 2010; Martire et al., 2010; Natalicchio et al., 2012). Some of the diagenetic carbonates in the underlying strata contain abundant ^{13}C-depleted molecular fossils (δ^{13}C values as low as −102‰) of a SD-AOM consortium (Natalicchio et al., 2012; Supplementary Table S1), confirming that carbonate precipitation was induced by SD-AOM. In
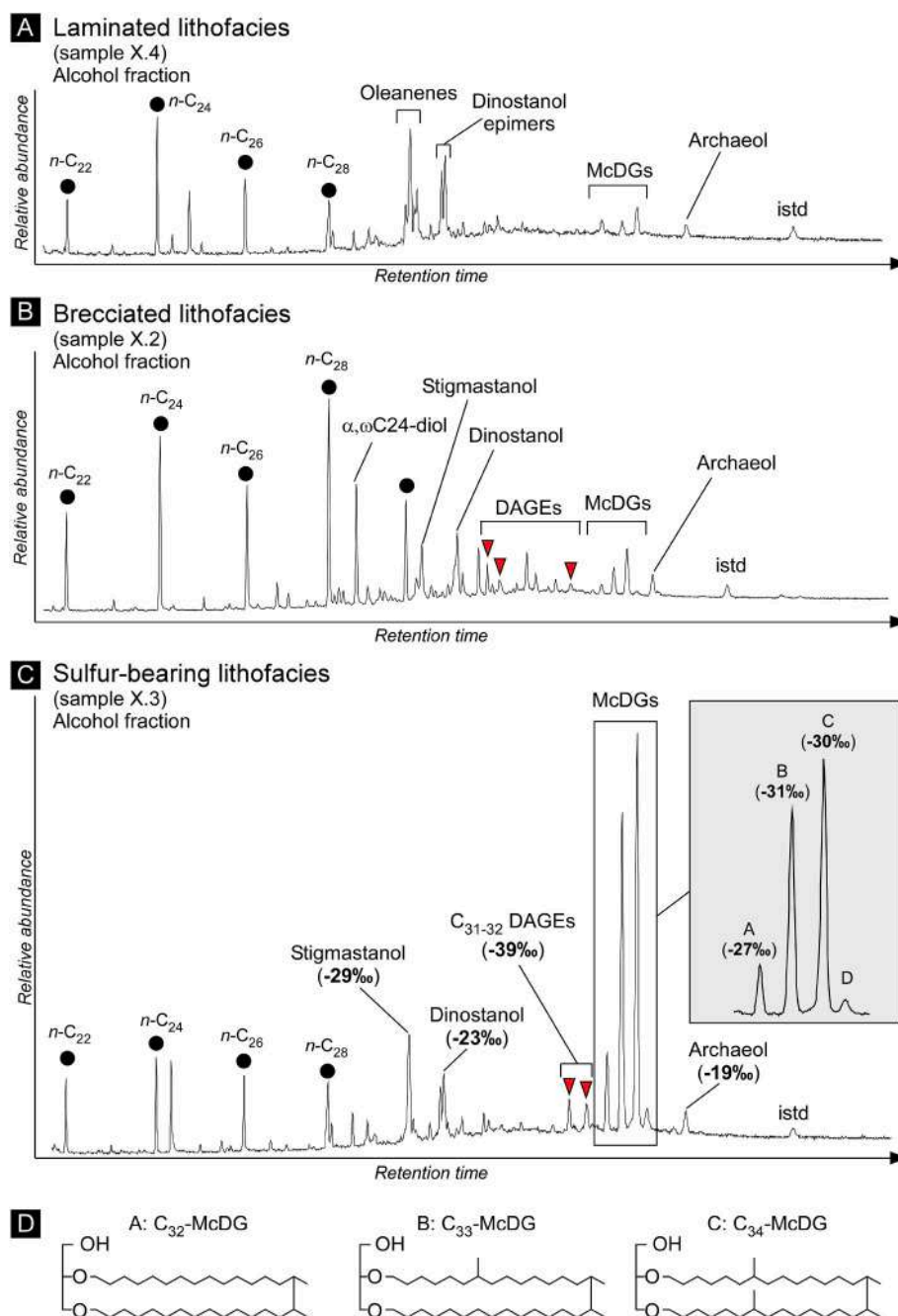
Fig. 8. Chromatograms of the laminated (A), brecciated (B) and sulfur-bearing (C) lithofacies showing the distribution and the relative abundance of the main lipids in the alcohol fraction. In C, compound specific carbon isotope values are also indicated for the most abundant lipids. D) Molecular structures of the main macrocyclic diethers (McDGs) with 32 (15,16-dimethyl-C_{30}), 33 (7, 15, 16-trimethyl-C_{30}) and 34 (7, 15, 16, 24-tetramethyl-C_{30}) carbons, respectively, attached to the glycerol via two ether bonds (see Baudrand et al., 2010 for details). ist: internal standard; DAGE: dialkyl glycerol diethers.

addition, these stratigraphically deeper authigenic carbonate rocks provide evidence of vertical displacements of the SMTZ based on the different types of formations arguably forming at different depths (see a complete list of molecular fossils of these concretions in Supplementary Table S1; cf. Dela Pierre et al., 2010; Natalicchio et al., 2012). Cylindrical concretions correspond to conduits originating by the upward migration of methane-rich fluids (Clari et al., 2009; Cavagna et al., 2015). Surprisingly, the similarly negative $\delta^{13}C$ values of the cement of the mud-filled fissures of the studied elemental sulfur-containing concretions are not accompanied by any molecular fossils indicative of SD-AOM. The only evidence for archaea is the presence of archaeol, a biomarker of many representatives of this domain of life (Koga et al.,

1998). However, the $\delta^{13}C$ value of archaeol of −19‰ and the absence of diagnostic SD-AOM lipids argue against the occurrence of this biogeochemical process in the depositional environment where the Ripa dello Zolfo concretions formed; therefore archaeol was rather sourced by methanogens, halophiles, or marine planktic Euryarchaeota (cf. Koga et al., 1998; Vandier et al., 2021; Sollai et al., 2019). Although diagnostic lipids of sulfate-reducing bacteria (terminally branched fatty acids and $C_{31/32}$ DAGEs) are present in the brecciated lithofacies, their compound-specific $\delta^{13}C$ values (−39‰) are also not consistent with SD-AOM and rather point to OSR. This line of evidence argues against the formation of the strongly ^{13}C-depleted calcite cement within the SMTZ by SD-AOM. A possible explanation for the ^{13}C-depleted
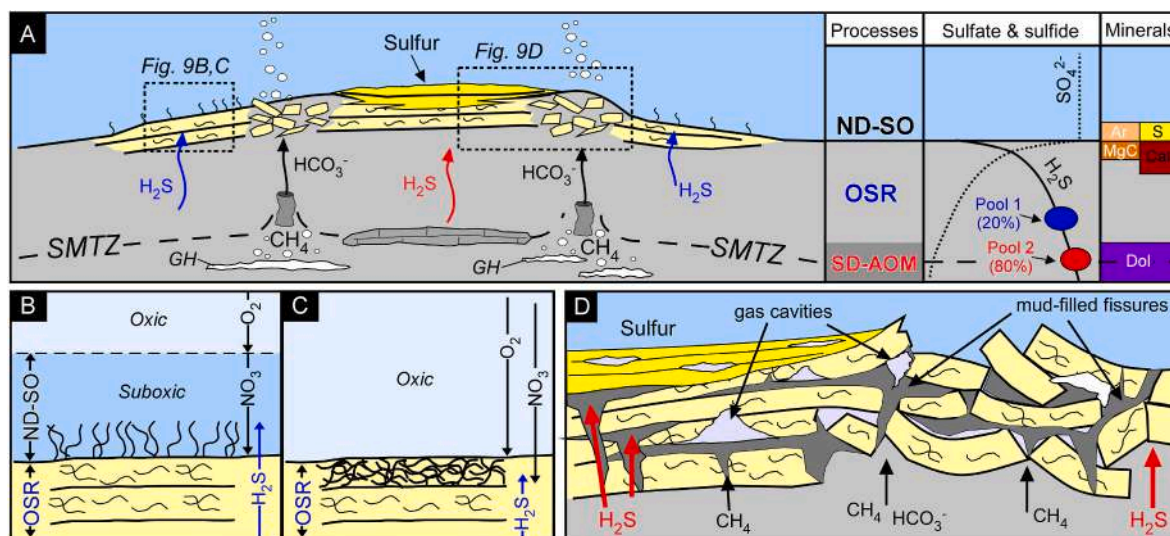
Fig. 9. A) Schematic scenario for the formation of the Ripa dello Zolfo carbonate and elemental sulfur. GH: gas hydrate. The columns on the right represent the suggested processes (OSR: organoclastic sulfate-reduction; SD-AOM: sulfate-driven anaerobic oxidation of methane; ND-SO: nitrate-driven sulfide oxidation), sulfate and sulfide profiles, two pools of H$_2$S (blue: within the OSR zone; red: at the SMTZ), and the authigenic minerals (Ar: aragonite; S: sulfur; MgC: Mg calcite; Cal: calcite; Dol: dolomite). B-D) Details of A showing the formation of the laminated (B, C) and the brecciated and sulfur-bearing (D) lithofacies. See text for details.

authigenic carbonate is the supply of SD-AOM-derived bicarbonate ions from a deep-seated SMTZ (Fig. 9A–D); the presence of stratabound and cylindrical methane-derived concretions cemented by dolomite (Natalicchio et al., 2012; Cavagna et al., 2015, Fig. 9A) a few meters below the studied sulfur-bearing concretion suggests that a SMTZ must have been present in the vicinity. Therefore, the SD-AOM-generated bicarbonate ions were apparently entrained with fluidized mud by upward rising overpressured fluids, shifting the carbonate equilibrium toward supersaturation and inducing the precipitation of ^{13}C-depleted low-Mg calcite in the pores of the mud filling the fissures. The positive δ^{18}O values of this cement may suggest that fluids were produced by gas hydrate destabilization (Dela Pierre et al., 2010). According to this scenario, gas-rich fluids escaping toward the water column were probably entrapped in partially cemented sediments giving rise to the cavernous fabric of the studied concretions (Fig. 4E and F; Fig. 9D). Cavities with angular edges were possibly originated by the growth of gas hydrates in the sediment and their subsequent destabilization. Similar features were described in modern (Bohrmann et al., 1998; Greinert et al., 2001) and ancient (Bojanowski, 2007; Martire et al., 2010) gas hydrate-associated carbonates.

5.3. Formation of the sulfur-bearing lithofacies

The observations that sulfur did not aggregate in a displacive mode, forming thin discontinuous laminae parallel to bedding and draping the breccia derived from the stromatolite suggests that sulfur is a syngenetic product of the oxidation of hydrogen sulfide at or close to the seafloor. Elongated cavities, probably derived from rising gas, are enclosed within the sulfur laminae (Fig. 5A–C), further supporting a shallow formation depth.

The sulfur isotope composition of elemental sulfur (δ^{34}S and Δ^{33}S) can be used to further distinguish whether hydrogen sulfide was produced by OSR or SD-AOM (Lin Z. et al., 2018; Liu et al., 2020, 2022). At the top of the microbial sulfate reduction zone, pore water is fed by seawater-derived sulfate diffusing from the water column into the sediments (δ^{34}S= 22.2 ± 0.2‰ and Δ^{33}S= 0.035 ± 0.013‰ for the Messinian seawater; Masterson et al., 2016); the hydrogen sulfide produced from its reduction yields much lower δ^{34}S (as low as −50‰) and higher Δ^{33}S values (as high as +0.2‰) than coeval oceanic sulfate (Johnston, 2011). With increasing depth, sulfate is progressively consumed by microbial sulfate reduction; the δ^{34}S values of hydrogen sulfide tend to

increase and Δ^{33}S values tend to decrease following a Rayleigh type distillation (Fike et al., 2015). In the vicinity of the SMTZ, where porewater sulfate is typically close to be completely consumed, the isotopic composition of hydrogen sulfide is often observed to be similar to that of seawater sulfate (Liu et al., 2020, 2022). Within or below the SMTZ, where trace amounts of sulfate are still present and methane diffuses upward from the methanic zone, OSR is outcompeted by SD-AOM and the resulting hydrogen sulfide is typically characterized by higher δ^{34}S and lower Δ^{33}S values than those of coeval seawater (Lin Z. et al., 2018; Liu et al., 2022).

The isotope values of the Ripa dello Zolfo native sulfur (δ^{34}S and Δ^{33}S) plot in a mixing area between two sulfur pools, i.e., sulfur derived from the oxidation of hydrogen sulfide produced by OSR and from SD-AOM (Fig. 7). We applied the numerical model described in paragraph 3.5 to trace the relative amount of sulfate that has been consumed in the porewater (controlled by the parameter f_{SO4} varying between 0 and 1), the contribution of two different hydrogen sulfide pools (controlled by the parameter f_{mix} varying between 0 and 1), and the process responsible for hydrogen sulfide oxidation. The results of this modelling exercise for biotic (i.e., chemolithotrophic) and abiotic oxidation are shown in Fig. 7A and **B,** respectively. In both diagrams (Fig. 7A and B), the isotope values of elemental sulfur plot in a relatively small area characterized by $f_{mix} \geq 0.8$. At least 80% of the reoxidized hydrogen sulfide to produce elemental sulfur derives from a porewater reservoir exhausted in sulfate, i.e., from the base of the microbial sulfate reduction zone, most likely in the surroundings of the SMTZ (Fig. 9A). The remaining 20% of hydrogen sulfide was produced by OSR at shallower sediment depth, where the porewater sulfate concentration was closer to its concentration in seawater. In particular, the fact that in both diagrams elemental sulfur values plot between $f_{SO4} = 0.2$ and $f_{SO4} = 0.4$ suggests that 60–80% of porewater sulfate was already consumed and reduced to hydrogen sulfide. Therefore, the elemental sulfur in the Ripa dello Zolfo concretions mostly derives from the oxidation of dissolved hydrogen sulfide produced at the vicinity of a deep-seated SMTZ. Interestingly, in the Ripa dello Zolfo concretions sulfur co-precipitated with ^{13}C-depleted authigenic calcite, probably reflecting carbonate supersaturation induced by the upward rising of ^{13}C-depleted bicarbonate ions originated in a deep-seated SMTZ and transported upward by overpressured fluids (Fig. 9D). The same mechanism may have been responsible for the upward transport of hydrogen sulfide. The latter was subsequently oxidized to elemental sulfur at or close to the seafloor, either abiotically or

biotically.

Both biotic and abiotic oxidation of hydrogen sulfide involve only limited isotope fractionation (Zerkle et al., 2016; Eldridge and Farquhar, 2018; Liu et al., 2020). Abiotic oxidation occurs with molecular oxygen or, in oxygen-depleted sediments like those studied here, with the concomitant reduction of iron oxides or nitrate (Lichtschlag et al., 2013; Lin Z. et al., 2018; Liu et al., 2020, 2022). Biotic oxidation is mediated by sulfide-oxidizing chemolithotrophs. Among them, *Arcobacter* is known to form elemental sulfur during bacterial oxidation of sulfide, forming dense "cotton-like" microbial mats at or immediately below the seafloor (Taylor and Wirsen, 1997; Wirsen et al., 2002; Sievert et al., 2007; Grünke et al., 2011; Madrid et al., 2001; Fischer et al., 2012; Pimenov et al., 2018). The results from the isotope model do not allow to discriminate whether the oxidation of sulfide was abiotic or biotic since the area representing chemolithotrophic oxidation (Fig. 7A) largely overlaps with the area reflecting abiotic oxidation (Fig. 7B).

While abiotic oxidation with metal oxides has been proposed to be the principal mechanisms for hydrogen sulfide oxidation in marine sediments from the Southern China and Baltic seas (Lin Z. et al., 2018; Liu et al., 2020, 2022), the absence of iron oxides and pyrite in the sulfur-bearing lithofacies argues against such process as the driving mechanism for elemental sulfur formation. In contrast, the involvement of microorganisms in the formation of elemental sulfur apparently agrees with the intense autofluorescence of the sulfur laminae, which suggest the presence of organic matter; the latter might represent the original, though degraded, biomass of the microorganisms involved in sulfide oxidation and sulfur precipitation, akin to the known sulfur-excreting bacteria. The molecular fossils assemblage of the sulfur-bearing lithofacies does not provide conclusive evidence on the involvement of such microorganisms. The most abundant molecular fossils of this lithofacies are short-chain C_{12-18} fatty acids, with a predominance of saturated and unsaturated C_{16} and C_{18} fatty acids. These lipids are indeed produced by modern sulfur-excreting bacteria (i.e., *Arcobacter*; Jelinek et al., 2006; Park et al., 2016; Zhang et al., 2016), but these compounds are also synthesized by many organisms including other filamentous sulfide-oxidizing bacteria (i.e., *Beggiatoa*; Arning et al., 2008).

Besides fatty acids, high contents of non-isoprenoid macrocyclic glycerol diethers (McDGs) were found in the Ripa dello Zolfo lithofacies, especially in the sulfur-bearing-lithofacies. Although the source of these compounds is enigmatic, McDGs have also been described from hydrothermal sulfidic environments (Blumenberg et al., 2007). The same McDGs like the Ripa dello Zolfo McDGs were found in sulfur-bearing carbonates deriving from diagenetic transformation of gypsum (Baudrand et al., 2010; Ziegenbalg et al., 2012; Aloisi et al., 2013; Birgel et al., 2014). Possible sources of the McDGs are extremophilic bacteria including sulfate-reducing bacteria adapted to extreme conditions (Rouwendaal et al., 2023). Interestingly, it has been suggested that sulfate-reducing bacteria may induce the precipitation of native sulfur under highly sulfidic conditions (Bishop et al., 2013; Labrado et al., 2019; Wang et al., 2023). In the sulfur-bearing lithofacies, the $\delta^{13}C$ signatures of McDGs are similar to the signatures of lipids from allochthonous sources such as algae or land plants (i.e., stigmastanol, dinostanol, cholesterol) but also sulfate-reducing bacteria (i.e., DAGE). Such values agree with a heterotrophic metabolism of the McDG-producing organisms. In this light, an origin of the Ripa dello Zolfo elemental sulfur from sulfate-reducing bacteria incompletely reducing sulfate to elemental sulfur as an adaptation to extreme environmental conditions – as opposed to sulfide oxidation to native sulfur – cannot be excluded (Rouwendaal et al., 2023).

6. Conclusions

Authigenic carbonate minerals and elemental sulfur hosted in early Messinian suboxic sediments originated as a consequence of organoclastic and methane-driven sulfate reduction. The former process promoted the formation of aphotic carbonate stromatolites from benthic microbial mats dominated by filamentous sulfide-oxidizing bacteria. Calcification was probably favored by nitrate-driven sulfide oxidation at the seafloor and organoclastic sulfate reduction at shallow sediment depth. Local overpressure, possibly induced by gas hydrate destabilization, promoted the brecciation of the carbonate stromatolites by mud injection and the upward transport of ^{13}C-depleted bicarbonate ions and ^{34}S-enriched hydrogen sulfide produced by sulfate-driven anaerobic oxidation of methane at a sulfate-methane transition zone at greater depth. The consequent alkalinity rise favored the precipitation of ^{13}C-depleted calcite, whereas the oxidation of hydrogen sulfide led to the formation of elemental sulfur at or close to the seafloor. Sulfide oxidation was possibly mediated by microorganisms such as sulfur excreting sulfide-oxidizing bacteria. Alternatively, sulfate-reducing bacteria adapted to locally extreme conditions reduced sulfate to elemental sulfur under highly sulfidic conditions. This study highlights that a multiproxy approach, including sedimentological and petrographical observations coupled with isotope geochemistry and lipid biomarkers, has great potential for the reconstruction of spatially and temporarily separated biogeochemical processes in the shallow subsurface or at the seafloor (i.e., anaerobic methane oxidation, sulfate reduction, sulfide oxidation) – processes that may induce the syngenetic formation of authigenic carbonate and sulfur deposits in marine sediments.

CRediT authorship contribution statement

M. Natalicchio: Writing – review & editing, Writing – original draft, Supervision, Methodology, Investigation, Funding acquisition, Data curation, Conceptualization. **D. Birgel:** Writing – review & editing, Writing – original draft, Methodology, Investigation, Formal analysis, Data curation. **S. Giunti:** Writing – review & editing, Investigation, Data curation. **L. Guibourdenche:** Writing – review & editing, Writing – original draft, Methodology, Formal analysis, Data curation. **L. Pellegrino:** Writing – review & editing, Validation, Investigation, Data curation. **G. Aloisi:** Writing – review & editing, Validation, Data curation. **J. Peckmann:** Writing – review & editing, Validation, Formal analysis. **F. Dela Pierre:** Writing – review & editing, Writing – original draft, Supervision, Methodology, Investigation, Funding acquisition, Data curation, Conceptualization.

Declaration of competing interest

The authors declare that they have no known competing financial interests or personal relationships that could have appeared to influence the work reported in this paper.

Data availability

Data will be made available on request.

Appendix A. Supplementary data

Supplementary data to this article can be found online at https://doi.

org/10.1016/j.marpetgeo.2024.106889.

References

Akam, S.A., Swanner, E., Yao, H., Hong, W.-L., Peckmann, J., 2023. Methane-derived authigenic carbonates – a case for a globally relevant marine carbonate factory. Earth Sci. Rev. 243, 104487.

Aloisi, G., Baudrand, M., Lécuyer, C., Rouchy, J.-M., Pancost, R.D., Aref, M.A.M., Grossi, V., 2013. Biomarker and isotope evidence for microbially-mediated carbonate formation from gypsum and petroleum hydrocarbons. Chem. Geol. 347, 199–207.

Aloisi, G., Guibourdenche, L., Natalicchio, M., Caruso, A., Haffert, L., El Kilany, A., Dela Pierre, F., 2022. The geochemical riddle of "low-salinity gypsum" deposits. Geochem. Cosmochim. Acta 327, 247–275.

Andreetto, F., Dela Pierre, F., Gibert, L., Natalicchio, M., Ferrando, S., 2019. Potential fossilized sulfide-oxidizing bacteria in the upper Miocene sulfur-bearing limestones from the Lorca Basin (SE Spain): Paleoenvironmental implications. Front. Microbiol. 10, 1031.

Arning, E.T., Birgel, D., Schulz-Vogt, H.N., Holmkvist, L., Jørgensen, B.B., Larson, A., Peckmann, J., 2008. Lipid biomarker patterns of phosphogenic sediments from upwelling regions. Geomicrobiol. J. 25, 69–82.

Arning, E.T., Birgel, D., Brunner, B., Peckmann, J., 2009. Bacterial formation of phosphatic laminites off Peru. Geobiology 7, 295–307.

Bailey, J.V., Orphan, V.J., Joye, S.B., Corsetti, F., 2009. Chemotrophic microbial mats and their potential for preservation in the rock record. Astrobiology 9, 843–859.

Baudrand, M., Grossi, V., Pancost, R., Aloisi, G., 2010. Non-isoprenoid macrocyclic glycerol diethers associated with authigenic carbonates. Org. Geochem. 41, 1341–1344.

Bellanca, A., Caruso, A., Ferruzza, G., Neri, R., Rouchy, J.M., Sprovieri, M., Blanc Valleron, M.M., 2001. Transition from marine to hypersaline conditions in the Messinian Tripoli Formation from the marginal areas of the central Sicilian Basin. Sediment. Geol. 140, 87105.

Berner, R.A., 1984. Sedimentary pyrite formation: an update. Geochem. Cosmochim. Acta 48, 605–615.

Bigi, G., Cosentino, D., Parotto, M., Sartori, R., Scandone, P., 1990. Structural model of Italy: Geodynamic Project: Consiglio Nazionale delle Ricerche, S.EL.CA. scale 1, 500, 000, sheet 1.

Birgel, D., Guido, A., Liu, X., Hinrichs, K.U., Gier, S., Peckmann, J., 2014. Hypersaline conditions during deposition of the Calcare di Base revealed from archaeal di-and tetraether inventories. Org. Geochem. 77, 11–21.

Birgel, D., Thiel, V., Hinrichs, K.-U., Elvert, M., Campbell, K.A., Reitner, J., Farmer, J.D., Peckmann, J., 2006. Lipid biomarker patterns of methane-seep microbialites from the Mesozoic convergent margin of California. Org. Geochem. 37, 1289–1302.

Birgel, D., Elvert, M., Han, X., Peckmann, J., 2008. ^{13}C-depleted biphytanic diacids as tracers of past anaerobic oxidation of methane. Org. Geochem. 39, 152–156.

Bishop, T., Turchyn, A.V., Sivan, O., 2013. Fire and brimstone: the microbially mediated formation of elemental sulfur nodules from an isotope and major element study in the Paleo-Dead Sea. PLoS One 8, e75883.

Blumenberg, M., Seifert, R., Reitner, J., Pape, T., Michaelis, W., 2004. Membrane lipid patterns typify distinct anaerobic methanotrophic consortia. Proc. Nat. Acad. Sci. 101, 11111–11116.

Blumenberg, M., Seifert, R., Petersen, S., Michaelis, W., 2007. Biosignatures present in a hydrothermal massive sulfide from the mid-Atlantic ridge. Geobiology 5, 435–450.

Boetius, A., Ravenschlag, K., Schubert, C.J., Rickert, D., Widdel, F., Gieseke, A., Amann, R., Jørgensen, B.B., Witte, U., Pfannkuche, O., 2000. A marine microbial consortium apparently mediating anaerobic oxidation of methane. Nature 407, 623–626.

Bohrmann, G., Torres, M.E., 2006. Gas hydrates in marine sediments. In: Schulz, H.D., Zabel, M. (Eds.), Marine Geochemistry. Springer, Berlin, pp. 481–512.

Bohrmann, G., Greinert, J.G., Suess, E., Torres, M., 1998. Authigenic carbonates and their relation to gas hydrate stability. Geology 26, 647–650.

Bojanowski, M.J., 2007. Oligocene cold-seep carbonates from the Carpathians and their inferred relation to gas hydrates. Facies 53, 347–360.

Borrelli, M., Perri, E., Critelli, S., Gindre-Chanu, L., 2021. The onset of the Messinian Salinity Crisis in the central Mediterranean recorded by pre-salt carbonate/evaporite deposition. Sedimentology 68, 1159–1197.

Brand, W.A., Coplen, T.B., Vogl, J., Rosner, M., Prohaska, T., 2014. Assessment of international reference materials for isotope-ratio analysis (IUPAC Technical Report). Pure Appl. Chem. 86, 425–467.

Caesar, K.H., Kyle, J.R., Lyons, T.W., Tripati, A., Loyd, S.J., 2019. Carbonate formation in salt dome cap rocks by microbial anaerobic oxidation of methane. Nat. Commun. 101, 808.

Campbell, K.A., 2006. Hydrocarbon seep and hydrothermal vent paleoenvironments and paleontology: past developments and future research directions. Palaeogeogr. Palaeoclimatol. Palaeoecol. 232, 362–407.

Caruso, A., Pierre, C., Blanc Valleron, M.M., Rouchy, J.M., 2015. Carbonate deposition and diagenesis in evaporitic environments: the evaporative and sulphur-bearing limestones during the settlement of the Messinian Salinity Crisis in Sicily and Calabria. Palaeogeogr. Palaeoclimatol. Palaeoecol. 429, 136–162.

Cavagna, S., Clari, P., Dela Pierre, F., Martire, L., Natalicchio, M., 2015. Sluggish and steady focussed flows through fine-grained sediments: the methane-derived cylindrical concretions of the Tertiary Piedmont Basin (NW Italy). Mar. Petrol. Geol. 66, 596–605.

Clari, P., Dela Pierre, F., Martire, L., Cavagna, S., 2009. The Cenozoic CH$_4$-derived carbonates of Monferrato (NW Italy): a solid evidence of fluid circulation in the sedimentary column. Mar. Geol. 265, 167–184.

Dawson, K.S., Freeman, K.H., Macalady, J.L., 2012. Molecular characterization of core lipids from halophilic archaea grown under different salinity conditions. Org. Geochem. 48, 1–8.

Dela Pierre, F., Martire, L., Natalicchio, M., Clari, P.A., Petrea, C., 2010. Authigenic carbonates in the upper Miocene sediments of the Tertiary Piedmont Basin (NW Italy): vestiges of an ancient gas hydrate stability zone. Geol. Soc. Am. Bull. 122, 994–1010.

Dela Pierre, F., Natalicchio, M., Ferrando, S., Giustetto, R., Birgel, D., Carnevale, G., Gier, S., Lozar, F., Marabello, D., Peckmann, J., 2015. Are the large filamentous microfossils preserved in Messinian gypsum colorless sulfide-oxidizing bacteria? Geology 43, 855–858.

Di Giulio, A., Galbiati, B., 1995. Interaction between tectonics and deposition into an episutural basin in the Alps-Apennine knot. In: Polino, R., Sacchi, R. (Eds.), Atti del Convegno Rapporti Alpi-Appennino: Accademia Nazionale delle Scienze detta dei XL, vol. 14. Scritti e Documenti, pp. 113–128.

Ding, T., Valkiers, S., Kipphardt, H., De Bièvre, P., Taylor, P.D.P., Gonfiantini, R., Krouse, R., 2001. Calibrated sulfur isotope abundance ratios of three IAEA sulfur isotope reference materials and V-CDT with a reassessment of the atomic weight of sulfur. Geochem. Cosmochim. Acta 65, 2433–2437.

Eldridge, D.L., Farquhar, J., 2018. Rates and multiple sulfur isotope fractionations associated with the oxidation of sulfide by oxygen in aqueous solution. Geochem. Cosmochim. Acta 237, 240–260.

Festa, A., Piana, F., Dela Pierre, F., Malusà, M.G., Mosca, P., Polino, R., 2005. Oligocene-Neogene kinematic constraints in the retroforeland basin of the Northwestern Alps. Rendicont. Soc. Geol. Ital. 1, 107–108.

Festa, A., Fioraso, G., Bissacca, E., Petrizzo, M.R., 2015. Geology of the Villalvernia–Varzi line between Scrivia and Curone valleys (NW Italy). J. Maps 11, 39–55.

Fike, D.A., Bradley, A.S., Rose, C.V., 2015. Rethinking the ancient sulfur cycle. Annu. Rev. Earth Planet Sci. 43, 593–622.

Fischer, D., Sahling, H., Nothen, K., Bohrmann, G., Zabel, M., Kasten, S., 2012. Interaction between hydrocarbon seepage, chemosynthetic communities, and bottom water redox at cold seeps of the Makran accretionary prism: insights from habitat-specific pore water sampling and modeling. Biogeosciences 9, 2013–2031.

Fossing, H., Jørgensen, B.B., 1989. Measurement of bacterial sulfate reduction in sediments: Evaluation of a single-step chromium reduction method. Biogeochemistry 8, 205–222.

Geng, L., Savarino, J., Savarino, C.A., Caillon, N., Cartigny, P., Hattori, S., Ishino, S., Yoshida, N., 2018. A simple and reliable method reducing sulfate to sulfide for multiple sulfur isotope analysis. Rapid Commun. Mass Spectrom. 32, 333–341.

Gennari, R., Manzi, V., Angeletti, A., Bertini, A., Biffi, U., Ceregato, A., Faranda, C., Gliozzi, E., Lugli, S., Menichetti, E., Rosso, A., Roveri, M., Taviani, M., 2013. A shallow water record of the onset of the Messinian salinity crisis in the Adriatic foredeep (Legnagnone section, Northern Apennines). Palaeogeogr. Palaeoclimatol. Palaeoecol. 386, 145–164.

Gennari, R., Lozar, F., Natalicchio, M., Zanella, E., Carnevale, G., Dela Pierre, F., 2020. Chronology of the Messinian events in the northernmost part of the Mediterranean: the Govone section (Piedmont Basin, NW Italy). Riv. Ital. Paleontol. Stratigr. 126, 541–560.

Ghibaudo, G., Clari, P., Perello, M., 1985. Litostratigrafia, sedimentologia ed evoluzione tettonicosedimentaria dei depositi miocenici del margine Sud-Orientale del Bacino Terziario Ligure-Piemontese (Valli Borbera, Scrivia e Lemme). Boll. Soc. Geol. Ital. 104, 349–397.

Greinert, J., Bohrmann, G., Suess, E., 2001. Gas hydrate-associated carbonates and methane-venting at Hydrate Ridge: classification, distribution, and origin of authigenic lithologies. In: Paull, C.K., Dillon, W.P. (Eds.), Natural Gas Hydrates: Occurrence, Distribution, and Detection. American Geophysical Union, Washington, pp. 99–113.

Grünke, S., Felden, J., Lichtschlag, A., Girnth, A.C., de Beer, D., Wenzhöfer, F., Boetius, A., 2011. Niche differentiation among mat-forming, sulfide-oxidizing bacteria at cold seeps of the Nile Deep Sea Fan (Eastern Mediterranean Sea). Geobiology 9, 330–348.

Guibourdenche, L., Cartigny, P., Dela Pierre, F., Natalicchio, M., Aloisi, G., 2022. Cryptic sulfur cycling during the formation of giant gypsum deposits. Earth Planet Sci. Lett. 593, 117676.

Himmler, T., Smrzka, D., Zwicker, J., Kasten, S., Shapiro, R.S., Bohrmann, G., Peckmann, J., 2018. Stromatolites below the photic zone in the northern Arabian Sea formed by calcifying chemotrophic microbial mats. Geology 46, 339–342.

Hsü, K.J., Cita, M.B., Ryan, W.B.F., 1973. The origin of the Mediterranean evaporites. In: Ryan, W.B.F., Hsü, K.J., et al. (Eds.), Initial Report of Deep Sea Drilling Program 13. U.S. Government Printing Office, Washington DC, pp. 1203–1231.

Irwin, H., Curtis, C., Coleman, M., 1977. Isotopic evidence for source of diagenetic carbonates formed during burial of organic-rich sediments. Nature 269, 209–213.

Jelinek, D., Miketova, P., Khailova, L., Schram, K.H., Moore, I.M., Vytřasová, J., 2006. Identification of *Arcobacter* species using phospholipid and total fatty acid profiles. Folia Microbiol. 51, 329–336.

Jessen, G.L., Lichtschlag, A., Struck, U., Boetius, A., 2016. Distribution and composition of thiotrophic mats in the hypoxic zone of the Black Sea (150–170 m water depth, Crimea margin). Front. Microbiol. 7, 1011.

Johnston, D.T., 2011. Multiple sulfur isotopes and the evolution of Earth's surface sulfur cycle. Earth Sci. Rev. 106, 161–183.

Johnston, D.T., Farquhar, J., Canfield, D.E., 2007. Sulfur isotope insights into microbial sulfate reduction: when microbes meet models. Geochem. Cosmochim. Acta 71, 3929–3947.

Jørgensen, B.B., 1982. Mineralization of organic matter in the sea bed—the role of sulphate reduction. Nature 296, 643–645.

Jørgensen, B.B., 2021. Sulfur biogeochemical cycle of marine sediments. Geochemical Perspectives 10, 145–146.

Jørgensen, B.B., Böttcher, M.E., Lüschen, H., Neretin, L.N., Volkov, I.I., 2004. Anaerobic methane oxidation and a deep H$_2$S sink generate isotopically heavy sulfides in Black Sea sediments. Geochem. Cosmochim. Acta 68, 2095–2118.

Jørgensen, B.B., Gallardo, V.A., 1999. *Thioploca* spp.: filamentous sulfur bacteria with nitrate vacuoles. FEMS (Fed. Eur. Microbiol. Soc.) Microbiol. Ecol. 28, 301–313.

Killops, S.D., Frewin, N.L., 1994. Triterpenoid diagenesis and cuticular preservation. Org. Geochem. 21, 1193–1209.

Koga, Y., Morii, H., Akagawa-Matsushita, M., Ohga, M., 1998. Correlation of polar lipid composition with 16S rRNA phylogeny in methanogens. Further analysis of lipid component parts. Biosci., Biotechnol., Biochem. 62, 230–236.

Labidi, J., Cartigny, P., Birck, J.L., Assayag, N., Bourrand, J.J., 2012. Determination of multiple sulfur isotopes in glasses: a reappraisal of the MORB δ^{34}S. Chem. Geol. 334, 189–198.

Labrado, A.L., Brunner, B., Bernasconi, S.M., Peckmann, J., 2019. Formation of large native sulfur deposits does not require molecular oxygen. Front. Microbiol. 10, 24.

Lichtschlag, A., Kamyshny Jr, A., Ferdelman, T.G., de Beer, D., 2013. Intermediate sulfur oxidation state compounds in the euxinic surface sediments of the Dvurechenskii mud volcano (Black Sea). Geochem. Cosmochim. Acta 105, 130–145.

Lin, Q., Wang, J., Fu, S., Lu, H., Bu, Q., Lin, R., Sun, F., 2015. Elemental sulfur in northern South China Sea sediments and its significance. Sci. China Earth Sci. 58, 2271–2278.

Lin, Z., Sun, X., Strauss, H., Lu, Y., Böttcher, M.E., Teichert, B.M.A., Gong, J., Xu, L., Lu, H., Peckmann, J., 2018. Multiple sulfur isotopic evidence for the origin of elemental sulfur in an iron-dominated gas hydrate-bearing sedimentary environment. Mar. Geol. 403, 271–284.

Lindtke, J., Ziegenbalg, S.B., Brunner, B., Rouchy, J.M., Pierre, C., Peckmann, J., 2011. Authigenesis of native sulphur and dolomite in a lacustrine evaporitic setting (Hellín basin, Late Miocene, SE Spain). Geol. Mag. 148, 655–669.

Liu, J., Pellerin, A., Izon, G., Wang, J., Antler, G., Liang, J., Su, P., Jørgensen, B.B., Ono, S., 2020. The multiple sulphur isotope fingerprint of a sub-seafloor oxidative sulphur cycle driven by iron. Earth Planet Sci. Lett. 536, 116165.

Liu, J., Pellerin, A., Wang, J., Rickard, D., Antler, G., Zhao, J., Wang, Z., Jørgensen, B.B., Ono, S., 2022. Multiple sulfur isotopes discriminate organoclastic and methane-based sulfate reduction by sub-seafloor pyrite formation. Geochem. Cosmochim. Acta 316, 309–330.

Londry, K.L., Jahnke, L.L., Des Marais, D.J., 2004. Stable carbon isotope ratios of lipid biomarkers of sulfate-reducing bacteria. Appl. Environ. Microbiol. 70, 745–751. https://doi.org/10.1128/AEM.70.2.745-751.2004.

Madrid, V.M., Taylor, G.T., Scranton, M.I., Chistoserdov, A.Y., 2001. Phylogenetic diversity of bacterial and archaeal communities in the anoxic zone of the Cariaco Basin. Appl. Environ. Microbiol. 67, 1663–1674.

Martire, L., Natalicchio, M., Petrea, C., Cavagna, S., Clari, P., Dela Pierre, F., 2010. Petrographic evidence of the past occurrence of gas hydrates in the Tertiary Piedmont Basin (NW Italy). Geo Mar. Lett. 30, 461–476.

Masterson, A.L., Wing, B.A., Paytan, A., Farquhar, J., Johnston, D.T., 2016. The minor sulfur isotope composition of Cretaceous and Cenozoic seawater sulfate. Paleoceanography 31, 779–788.

McCaffrey, M.A., Farrington, J.W., Repeta, D.J., 1989. Geochemical implications of the lipid composition of *Thioploca* spp. from the Peru upwelling region—15 S. Org. Geochem. 14, 61–68.

Mosca, P., Polino, R., Rogledi, S., Rossi, M., 2010. New data for the kinematic interpretation of the Alps–Apennines junction (Northwestern Italy). Int. J. Earth Sci. 99, 833–849.

Natalicchio, M., Birgel, D., Dela Pierre, F., Martire, L., Clari, P., Spötl, C., Peckmann, J., 2012. Polyphasic carbonate precipitation in the shallow subsurface: insights from microbially-formed authigenic carbonate beds in upper Miocene sediments of the Tertiary Piedmont Basin (NW Italy). Palaeogeogr. Palaeoclimatol. Palaeoecol. 329, 158–172.

Natalicchio, M., Dela Pierre, F., Clari, P., Birgel, D., Cavagna, S., Martire, L., Peckmann, J., 2013. Hydrocarbon seepage during the Messinian salinity crisis in the Tertiary Piedmont Basin (NW Italy). Palaeogeogr. Palaeoclimatol. Palaeoecol. 390, 68–80.

Oliveri, E., Neri, R., Bellanca, A., Riding, R., 2010. Carbonate stromatolites from a Messinian hypersaline setting in the Caltanissetta Basin, Sicily: petrographic evidence of microbial activity and related stable isotope and rare earth element signatures. Sedimentology 57, 142–161.

Omoregie, E.O., Mastalerz, V., de Lange, G., Straub, K.L., Kappler, A., Røy, H.A., Foucher, J.P., Boetius, A., 2008. Biogeochemistry and community composition of iron-and sulfur-precipitating microbial mats at the Chefren mud volcano (Nile Deep Sea Fan, Eastern Mediterranean). Appl. Environ. Microbiol. 74, 3198–3215.

Omoregie, E.O., Niemann, H., Mastalerz, V., de Lange, G.J., Stadnitskaia, A., Mascle, J., Foucher, J.P., Boetius, A., 2009. Microbial methane oxidation and sulfate reduction at cold seeps of the deep Eastern Mediterranean Sea. Mar. Geol. 261, 114–127.

Ono, S., Wing, B., Johnston, D., Farquhar, J., Rumble, D., 2006. Mass-dependent fractionation of quadruple sulfur isotope system as a new tracer of sulfur biogeochemical cycles. Geochem. Cosmochim. Acta 70, 2238–2252.

Park, S., Jung, Y.T., Kim, S., Yoon, J.H., 2016. *Arcobacter acticola* sp. nov., isolated from seawater on the East Sea in South Korea. J. Microbiol. 54, 655–659.

Peckmann, J., Thiel, V., 2004. Carbon cycling at ancient methane-seeps. Chem. Geol. 205, 443–467.

Peckmann, J., Paul, J., Thiel, V., 1999. Bacterially mediated formation of diagenetic aragonite and native sulfur in Zechstein carbonates (Upper Permian, Central Germany). Sediment. Geol. 126, 205–222.

Peckmann, J., Thiel, V., Reitner, J., Taviani, M., Aharon, P., Michaelis, W., 2004. A microbial mat of a large sulfur bacterium preserved in a Miocene methane-seep limestone. Geomicrobiol. J. 21, 247–255.

Peckmann, J., Kiel, S., Sandy, M.R., Taylor, D.G., Goedert, J.L., 2011. Mass occurrences of the brachiopod *Halorella* in Late Triassic methane-seep deposits, eastern Oregon. J. Geol. 119, 207–220.

Pellegrino, L., Dela Pierre, F., Jordan, R.W., Abe, K., Mikami, Y., Natalicchio, M., Gennari, R., Lozar, F., Carnevale, G., 2020. The upper Miocene diatomaceous sediments of the northernmost Mediterranean region: a lamina-scale investigation of an overlooked palaeoceanographic archive. Sedimentology 67, 3389–3421.

Perri, E., Gindre-Chanu, L., Caruso, A., Cefalà, M., Scopelliti, G., Tucker, M., 2017. Microbial mediated pre-salt carbonate deposition during the Messinian salinity crisis (Calcare di Base fm., Southern Italy). Mar. Petrol. Geol. 88, 235–250.

Pierre, C., Rouchy, J.M., 2004. Isotopic compositions of diagenetic dolomites in the Tortonian marls of the Western Mediterranean margins: evidence of past gas hydrate formation and dissociation. Chem. Geol. 205, 469–484.

Pimenov, N.V., Merkel, A.Y., Tarnovetskii, I.Y., Malakhova, T.V., Samylina, O.S., Kanapatskii, T.A., Tikhonova, E.N., Vlasova, M.A., 2018. Structure of microbial mats in the Mramornaya Bay (Crimea) coastal areas. Microbiology 87, 681–691.

Rampen, S.W., Friedl, T., Rybalka, N., Thiel, V., 2022. The Long Chain Diol Index: a Marine Palaeotemperature Proxy Based on Eustigmatophyte Lipids that Record the Warmest Seasons. Proceedings of the National Academy of Sciences 119, e2116812119.

Ritger, S., Carson, B., Suess, E., 1987. Methane-derived authigenic carbonates formed by subduction-induced pore-water expulsion along the Oregon/Washington margin. Geol. Soc. Am. Bull. 98, 147–156.

Robinson, B.W., 1995. Sulphur isotope standards. Reference and Intercomparison materials for stable isotopes of light Elements. International Atomic Energy Agency Tecdoc 825, 39–46.

Rossi, M., 2017. Outcrop and seismic expression of stratigraphic patterns driven by accommodation and sediment supply turnarounds: implications on the meaning and variability of unconformities in syn-orogenic basins. Mar. Petrol. Geol. 87, 112–127.

Rouchy, J.M., Taberner, C., Blanc-Valleron, M.M., Sprovieri, R., Russell, M., Pierre, C., Di Stefano, E., Pueyo, J.J., Caruso, A., Dinarès-Turell, J., Gomis-Coll, E., Wolff, G.A., Cespuglio, G., Ditchfield, P., Pestrea, S., Santisteban, C., Grimalt, J.O., 1998. Sedimentary and diagenetic markers of the restriction in a marine basin: the Lorca Basin (SE Spain) during the Messinian. Sediment. Geol. 121, 23–55.

Rouwendaal, S.E., Birgel, D., Grossi, V., Aloisi, G., Guibourdenche, L., Labrado, A.L., Brunner, B., Rouchy, J.M., Peckmann, J., 2023. Two modes of gypsum replacement by carbonate and native sulfur in the Lorca Basin, SE Spain. Front. Earth Sci. 11, 1153415.

Ryan, W.B., 2023. 50th anniversary review of the Mediterranean desiccation hypothesis. La Rivista del Nuovo Cimento 1–129.

Sabino, M., Schefuß, E., Natalicchio, M., Dela Pierre, F., Birgel, D., Bortels, D., Schnetger, B., Peckmann, J., 2020. Climatic and hydrologic variability in the northern Mediterranean across the onset of the Messinian salinity crisis. Palaeogeogr. Palaeoecol. 545, 109632.

Sabino, M., Dela Pierre, F., Natalicchio, M., Birgel, D., Gier, S., Peckmann, J., 2021. The response of water column and sedimentary environments to the advent of the Messinian salinity crisis: insights from an onshore deep-water section (Govone, NW Italy). Geol. Mag. 158, 825–841.

Sahling, H., Rickert, D., Lee, R.W., Linke, P., Suess, E., 2002. Macrofaunal community structure and sulfide flux at gas hydrate deposits from the Cascadia convergent margin, NE Pacific. Mar. Ecol. Prog. Ser. 231, 121–138.

Schopf, J.W., Farmer, J.D., Foster, I.S., Kudryavtsev, A.B., Gallardo, V.A., Espinoza, C., 2012. Gypsum-permineralized microfossils and their relevance to the search for life on Mars. Astrobiology 12, 619–633.

Sievert, S.M., Wieringa, E.B., Wirsen, C.O., Taylor, C.D., 2007. Growth and mechanism of filamentous-sulfur formation by Candidatus *Arcobacter sulfidicus* in opposing oxygen-sulfide gradients. Environ. Microbiol. 9, 271–276.

Sollai, M., Villanueva, L., Hopmans, E.C., Keil, R.G., Sinninghe Damsté, J.S., 2019. Archaeal sources of intact membrane lipid biomarkers in the oxygen deficient zone of the eastern tropical South Pacific. Front. Microbiol. 10, 765.

Taylor, C.D., Wirsen, C.O., 1997. Microbiology and ecology of filamentous sulfur formation. Science 277, 1483–1485.

Taylor, C.D., Wirsen, C.O., Gaill, F., 1999. Rapid microbial production of filamentous sulfur mats at hydrothermal vents. Appl. Environ. Microbiol. 65, 2253–2255.

Teske, A., Nelson, D.C., 2006. The genera *Beggiatoa* and *Thioploca*. Prokaryotes 6, 784–810.

Tzevahirtzian, A., Caruso, A., Scopelliti, G., Baudin, F., Blanc Valleron, M.M., 2022. Onset of the Messinian salinity crisis: sedimentological, petrographic and geochemical characterization of the pre-salt sediments from a new core (Caltanissetta basin, Sicily). Mar. Petrol. Geol. 141, 105686.

Vandier, F., Tourte, M., Doumbe-Kingue, C., Plancq, J., Schaeffer, P., Oger, P., Grossi, V., 2021. Reappraisal of archaeal C$_{20}$-C$_{25}$ diether lipid (extended archaeol) origin and use as a biomarker of hypersalinity. Org. Geochem. 159, 104276.

Violanti, D., 1996. Palaeoautecological analysis of *Bulimina echinata* (Messinian, Mediterranean area). Boll. Soc. Paleontol. Ital. 3, 243–253.

Volkman, J.K., 2003. Sterols in microorganisms. Appl. Microbiol. Biotechnol. 60, 495–506.

Wang, S., Lu, Q., Liang, Z., Yu, X., Lin, M., Mai, B., Qiu, R., Shu, W., He, Z., Wall, J.D., 2023. Generation of Zero-Valent Sulfur from Dissimilatory Sulfate Reduction in Sulfate-Reducing Microorganisms. Proceedings of the National Academy of Sciences 120, e2220725120.

Wirsen, C.O., Sievert, S.M., Cavanaugh, C.M., Molyneaux, S.J., Ahmad, A.T.L.T., Taylor, L.T., Delong, E.F., Taylor, C.D., 2002. Characterization of an autotrophic sulfide-oxidizing marine *Arcobacter* sp. that produces filamentous sulfur. Appl. Environ. Microbiol. 68, 316–325.

Zerkle, A.L., Jones, D.S., Farquhar, J., Macalady, J.L., 2016. Sulfur isotope values in the sulfidic Frasassi cave system, central Italy: a case study of a chemolithotrophic S-based ecosystem. Geochem. Cosmochim. Acta 173, 373–386.

Zhang, Z., Yu, C., Wang, X., Yu, S., Zhang, X.H., 2016. *Arcobacter pacificus* sp. nov., isolated from seawater of the South Pacific Gyre. Int. J. Syst. Evol. Microbiol. 66, 542–547.

Ziegenbalg, S.B., Brunner, B., Rouchy, J.M., Birgel, D., Pierre, C., Böttcher, M.E., Caruso, A., Immenhauser, A., Peckmann, J., 2010. Formation of secondary carbonates and native sulphur in sulphate-rich Messinian strata, Sicily. Sediment. Geol. 227, 37–50.

Ziegenbalg, S.B., Birgel, D., Hoffmann-Sell, L., Pierre, C., Rouchy, J.M., Peckmann, J., 2012. Anaerobic oxidation of methane in hypersaline Messinian environments revealed by ^{13}C-depleted molecular fossils. Chem. Geol. 292, 140–148.